

**UNDERSTANDING HUMINS:
MOLECULAR CHARACTERIZATION
AND GROWTH RATES**

by

Michael Julian Orella

A thesis submitted to the Faculty of the University of Delaware in partial fulfillment of the requirements for the degree of Honors Bachelor of Chemical Engineering with Distinction

Spring 2014

© 2014 Michael Julian Orella
All Rights Reserved

**UNDERSTANDING HUMINS:
MOLECULAR CHARACTERIZATION
AND GROWTH RATES**

by

Michael Julian Orella

Approved: _____
Dionisios G. Vlachos, Ph.D.
Professor in charge of thesis on behalf of the Advisory Committee

Approved: _____
Vladimiro Nikolakis, Ph.D.
Committee member from the Department of Chemical and Biomolecular
Engineering

Approved: _____
Susan Groh, Ph.D.
Committee member from the Board of Senior Thesis Readers

Approved: _____
Michael Arnold, Ph.D.
Director, University Honors Program

ACKNOWLEDGMENTS

There are many people that I wish to thank for the help they have given me with completing this work. Without many of these people, I would not have been able to complete this work to the extent of my satisfaction and ability.

The first person I would like to thank is Dr. Vlachos who welcomed me to research in his labs starting my freshman year. With this opportunity, my eyes were opened to the wealth of knowledge that could be uncovered from research experience. He has helped me in all aspects of my undergraduate career, and I would not be where I am today without his guidance.

Next, I would like to thank Dr. George Tsilomelekis who was my research mentor for my thesis project. George taught me everything I needed to know and more about research in general, and about spectroscopy in particular. I was always excited to come into lab and ask questions of George to hear about his new ideas. Without George's guidance and mentorship, I doubt this project would be where it is at this point in time.

I would additionally like to thank Dr. Vlad Nikolakis for his efforts to educate me in research skills. I learned more technical skills from Vlad than I ever thought would be possible. Vlad was completely open to any questions and provide a critique whenever necessary. I always felt encouraged to bounce ideas off of George and Vlad, no matter how good or bad they may have been in the long run. This alone helped me grow as a researcher more than anything else in my undergraduate career, and I owe it to them completely.

I would also like to thank Dr. Vinit Choudhary, my first undergraduate research mentor, for getting me interested in research initially. I would like to thank Dr. Marta Leon-Garcia for always being willing to help me fix the HPLC when it was broken. Lastly I want to thank Dr. Susan Groh for her insightful questions during our thesis review meetings. Without her, and all of my other UD professors, I would never have even considered taking the opportunity to write this thesis, and would have missed out on all of the experiences that this has provided me.

TABLE OF CONTENTS

LIST OF TABLES	v
LIST OF FIGURES	vi
ABSTRACT	ix
1 INTRODUCTION	1
1.1 Background.....	1
1.2 Previous Literature	5
1.2.1 Electrophilic attack of HMF.....	6
1.2.2 Aldol addition/condensation of HMF.....	7
1.2.3 Nucleophilic attack on α and β furanolic positions.....	11
1.3 Structure of Thesis.....	12
1.4 Motivation	12
1.5 Goals of Thesis Work	13
1.5.1 Understanding Molecular Structure	13
1.5.2 Predicting Growth Rate	14
2 EXPERIMENTAL DESIGN	15
2.1 Materials	15
2.2 Infrared Spectroscopy (IR).....	15
2.2.1 Normalization of Spectra.....	15
2.3 Dynamic Light Scattering.....	16
2.4 High Performance Liquid Chromatography	17
2.5 Preparation Procedure	17
2.5.1 Batch Reactors.....	18
2.5.2 Washing Humins	18
3 STRUCTURAL IMPLICATIONS OF VIBRATIONAL SPECTROSCOPY MEASUREMENTS	19
3.1 Basics of Vibrational Spectroscopy.....	19

3.2	Establishment of Humin Processing Protocol	20
3.3	IR Spectra	25
3.3.1	ATR-FTIR of Humins and Vibrational Assignments	26
3.3.2	Effect of Starting Material on Humins' Structure	27
3.4	Validity of Proposed Structures.....	29
3.5	Dependence of Humin Structure on Conversion.....	34
3.6	Conclusions from Molecular Characterization.....	35
4	GROWTH RATE OF HUMIN PARTICLES	37
4.1	<i>In Situ</i> Light Scattering Kinetic Data	37
4.2	Autocorrelation Results	39
4.3	Autocorrelation Fit Methods	40
4.4	Kinetics of Humin Growth	45
5	FUTURE WORK AND CONCLUSIONS.....	54
	REFERENCES	56
A	BUFFER PREPARATION	59
B	HPLC CALIBRATION CURVES	60
C	THEORY OF INFRARED SPECTROSCOPY	63
D	FTIR VIBRATIONAL TABLES	65
E	THEORETICAL BACKGROUND OF DYNAMIC LIGHT SCATTERING	68
F	AUTOCORRELATION FUNCTIONS	70
F.1	T = 70°C	71
F.2	T = 60°C	73
F.3	T = 50°C	75

LIST OF TABLES

Table 3.1:	Example characteristic vibrations for the carbonyl functional group.	20
Table 3.2:	Infrared bands observed experimentally, and that should be observed based on the proposed structures of Weckhuysen [18], Lund [19, 20], and Sumerskii [21]	30
Table 4.1:	Operating conditions used for the <i>in situ</i> DLS studies.....	37
Table 4.2:	Conversion of HMF in each of the DLS experiments.....	38
Table 4.3:	Yield to formic acid from HMF in DLS experiments.	38
Table 4.4:	Yield to levulinic acid from HMF in DLS experiments.....	38
Table 4.5:	Reaction time used in DLS experiments.	38
Table 4.6:	Apparent activation energy measured from dynamic light scattering experiments.	51
Table 4.7:	Growth rate of humin particles as measured in replicate experiments. Error bars correspond to 95% confidence intervals.	53
Table A.1:	Buffer recipe for HCl/KCl buffer used in FTIR experiments.	59
Table D.1:	Carbonyl band vibrational frequencies.....	65
Table D.2:	Alkane band vibrational frequencies.	66
Table D.3:	Alkyne band vibrational frequencies.....	66
Table D.4:	Alcohol band vibrational frequencies.....	67
Table D.5:	Ether/acetal band vibrational frequencies.	67

LIST OF FIGURES

Figure 1.1: Possible products that can be synthesized from HMF.	2
Figure 1.2: Reaction scheme for cellulose to p-xylene as studied by the Catalysis Center for Energy Innovation.....	3
Figure 1.3: Humin formation scheme proposed by Horvat	4
Figure 1.4: Mechanism for electrophilic addition to aldehyde carbon suggested by Sumerskii et al.	6
Figure 1.5: Acetal structure proposed by Sumerskii et al. as being the linkages that form humins.	7
Figure 1.6: Structure proposed by Lund for aldol addition of HMF to DHH where each addition is just as fast as the first.	8
Figure 1.7: Structure proposed by Lund for aldol addition of HMF to DHH where the second addition is much slower than the first.	8
Figure 1.8: Suggested mechanism detailing the formation of a molecule of DHH and aldol addition of a single HMF molecule to it.....	10
Figure 1.9: The structure for humins resulting from nucleophilic attack of α and β carbons of HMF by all other compounds present in reaction mixture....	11
Figure 2.1: Procedure followed for humin production and characterization.	18
Figure 3.1: pH of aqueous wash versus volume used during the washing procedure.	21
Figure 3.2: Effect of washing humins on the SR - IR spectrum	22
Figure 3.3: Comparison of humins before and after washing with the starting materials and products of reaction.....	25
Figure 3.4: Example spectrum of 30% HMF humins in pH 1.1 buffer. Certain spectral characteristics are noted because of their importance in deducing structures of the humins.....	27

Figure 3.5: Effect of sugar on humin structure.	28
Figure 3.6: Humin structure proposed by Weckhuysen, where bonds are labelled according to the frequency they should have in the infrared spectrum. ..	31
Figure 3.7: Humin structure proposed by Lund when the rate of addition slows down upon each HMF addition.	32
Figure 3.8: Humin structure proposed by Lund when the rate of addition does not change.	33
Figure 3.9: Humin structure proposed by Sumerskii.	33
Figure 3.10: Humin structure as a function of conversion at 125°C.	34
Figure 4.1: Example autocorrelation functions for a typical DLS experiment.	39
Figure 4.2: Example of using the Brookhaven Instruments software for analysis of the DLS measurements.	42
Figure 4.3: Example autocorrelation function with bimodal distribution.	43
Figure 4.4: Example autocorrelation function where the autocorrelation data is not good and the fit is poor.	44
Figure 4.5: Bimodal particle size distribution example.	45
Figure 4.6: Dependence of humin growth rate on temperature at pH 1.0.	47
Figure 4.7: Dependence of humin growth rate on temperature at pH 0.5.	47
Figure 4.8: Dependence of humin growth rate on temperature at pH 0.0.	48
Figure 4.9: Correlation for humin induction time.	49
Figure 4.10: Humin linear growth rates correlated with reaction conditions.	50
Figure 4.11: Arrhenius plot of DLS experiments.	51
Figure 4.12: Replicate data for the DLS experiment at pH 1.0 and 50°C.	53
Figure B.1: HPLC calibration for formic acid.	60
Figure B.2: HPLC calibration for fructose.	61

Figure B.3: HPLC calibration for levulinic acid.	61
Figure B.4: HPLC calibration for glucose.....	62
Figure B.5: HPLC calibration for HMF.	62
Figure F.1: Autocorrelation function of humins produced at 70°C and pH 1.0.....	71
Figure F.2: Autocorrelation function of humins produced at 70°C and pH 0.5.....	72
Figure F.3: Autocorrelation function of humins produced at 70°C and pH 0.0.....	72
Figure F.4: Autocorrelation function of humins produced at 60°C and pH 1.0.....	73
Figure F.5: Autocorrelation function of humins produced at 60°C and pH 0.5.....	74
Figure F.6: Autocorrelation function of humins produced at 60°C and pH 0.0.....	74
Figure F.7: Autocorrelation function of humins produced at 50°C and pH 1.0.....	75
Figure F.8: Autocorrelation function of humins produced at 50°C and pH 1.0.....	76
Figure F.9: Autocorrelation function of humins produced at 50°C and pH 1.0.....	76
Figure F.10: Autocorrelation function of humins produced at 50°C and pH 0.5.....	77
Figure F.11: Autocorrelation function of humins produced at 50°C and pH 0.0.....	77

ABSTRACT

Dynamic light scattering (DLS) and *ex situ* Fourier transform infrared spectroscopy (FTIR) experimental techniques were utilized to investigate growth rates and chemical structure of humins formed during biomass conversion.

We show experimental proof that a rigorous procedure is needed to remove adsorbed products from the humin structure. These products consist mostly of 5-hydroxymethylfurfural (HMF), levulinic acid (LA), and formic acid (FA). We also demonstrate the difference in humin structure observed when humins are formed from HMF, fructose, or glucose. This difference is mainly observed in a new peak that appears at 1650 cm^{-1} that is ascribed to HMF incorporated in the humins. This peak is consumed over the course of the reaction, and at 100% conversion of HMF the peak disappears entirely. Lastly, we fit humin structures proposed in the literature to the FTIR data we collected, and find that the structures proposed by Lund et al. and by Weckhuysen et al. appear to be the most consistent with our data.

A novel experimental technique measuring humin formation was developed by using *in situ* DLS. We have been able to measure the activation energy of humin formation directly with this technique, and found activation energies between 18 – 55 kJ/mol. We attribute the differences between our measured values and previously reported values mostly to transport limitations in the DLS cell.

The results from these two studies need to be synthesized further via increased physical and chemical mechanistic understanding.

Chapter 1

INTRODUCTION

1.1 Background

Sustainable energy production has received renewed academic interest in recent years due to the propensity of predictions suggesting depleting sources of fossil fuels. In addition, demand for petroleum and other fuels is expected to increase 30% over the next two decades [1]. This demand, driven largely by the growing economies of India and China, is most promisingly accounted for by biomass feedstock sources [2]. Carbohydrates are an especially attractive option for biomass feedstock development because they are the most abundant natural carbon source [2]. The U.S. alone annually produces 1.3 billion tons of dry biomass [1]. The U.S. Department of Energy has even recognized the challenges with sustainable energy production from biomass feedstock, and has created an energy frontier research center (EFRC) called the Catalysis Center for Energy Innovation (CCEI) to study them [3]. In addition to providing a suitable alternative to fuel production, biomass derived compounds have the added benefit of being easily converted to value-added chemicals. Two examples of these value added chemicals include levulinic acid, which can be used for the bulk synthesis of many organic molecules [4, 5] and 5-hydroxymethylfurfural(HMF), which can be used for synthesis of chemicals [6], fuels [7], and monomeric units of polymers [8-10]. Because of the versatility of HMF, it is considered to be a “top” value added chemical [11]. Van Putten [2] et al. demonstrate the wide range of products that originate from HMF, shown in Figure 1.1.

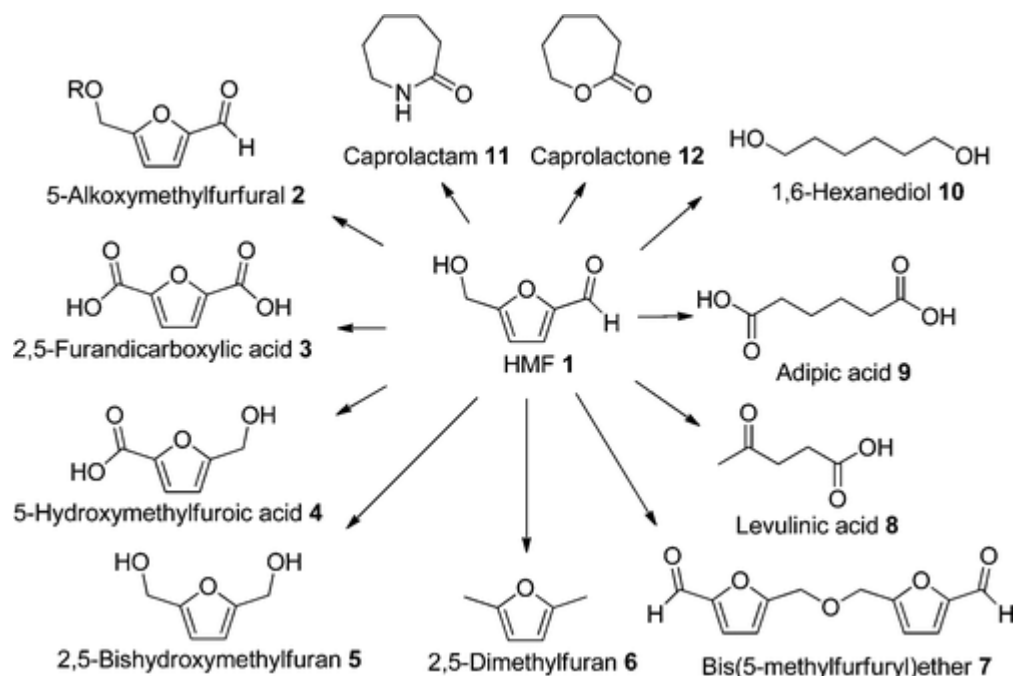


Figure 1.1: Possible products that can be synthesized from HMF.

The production of the six carbon HMF is typically completed by acid catalysis of fructose or glucose, which are obtained from cellulosic biomass sources. Cellulose can be dissolved in ionic liquids, so that solid acid catalysts can be used to hydrolyze the polymer into the monomer, glucose [12]. Glucose is the building block on which most of the sugar chemistry that the CCEI studies is derived [3]. Glucose can be isomerized to the more active hexose, fructose, by Lewis acid catalysis [13]. The fructose is then dehydrated under acidic conditions to form HMF [13]. The overall scheme for the production of valuable products from biomass that is followed by the CCEI [3] is shown in Figure 1.2, below.

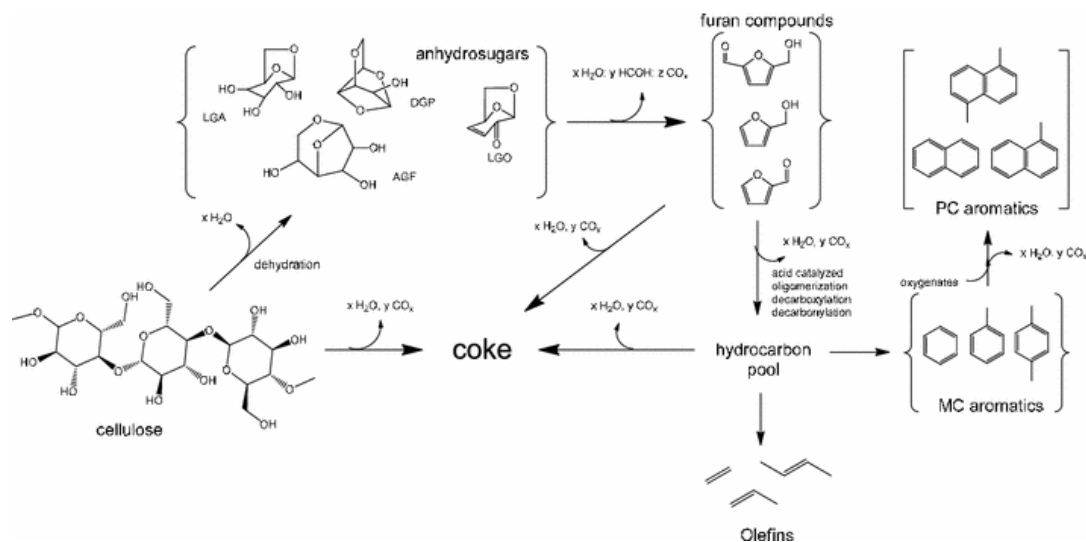


Figure 1.2: Reaction scheme for cellulose to p-xylene as studied by the Catalysis Center for Energy Innovation [3]. The reactions are catalyzed by either Brønsted or Lewis acids in a homogenous mixture, or on metal sites.

Typical yields of HMF during the fructose dehydration reaction are nearly 50% [2, 14]. These low yields are the result of formation of levulinic and formic acid under reaction conditions, as well as the formation of low value, insoluble waste called humins. Román et al. have suggested ways to increase the yields to HMF by operating in a biphasic system [14], which stabilizes the HMF against side reactions. We are just beginning to understand the fundamental basis for the increased stability of HMF in non-aqueous solvents [15]. Although we can increase the yield to HMF, we still do not have the fundamental understanding of humins or their formation mechanism to hinder their growth. An in depth economic study of biomass production was completed that suggested that increased selectivity to HMF was a key parameter of the process economics [16]. By eliminating the formation of humins, the selectivity to HMF can drastically be improved, which will aid the economics greatly. A more detailed

description of the problems that humin formation cause, and the motivation behind this study will be discussed in Section 1.4.

The first attempt to classify humins was in a 1985 article by Horvat, where his group suggests that HMF undergoes an addition adjacent to the alkoxy group to form the precursor to humins [17]. In this scheme, Horvat depicts the addition of water to HMF to form levulinic acid, and the addition to form 2,5-dioxo-6-hydroxyhexanal (DHH). The scheme that Horvat suggests is shown in Figure 1.3, below.

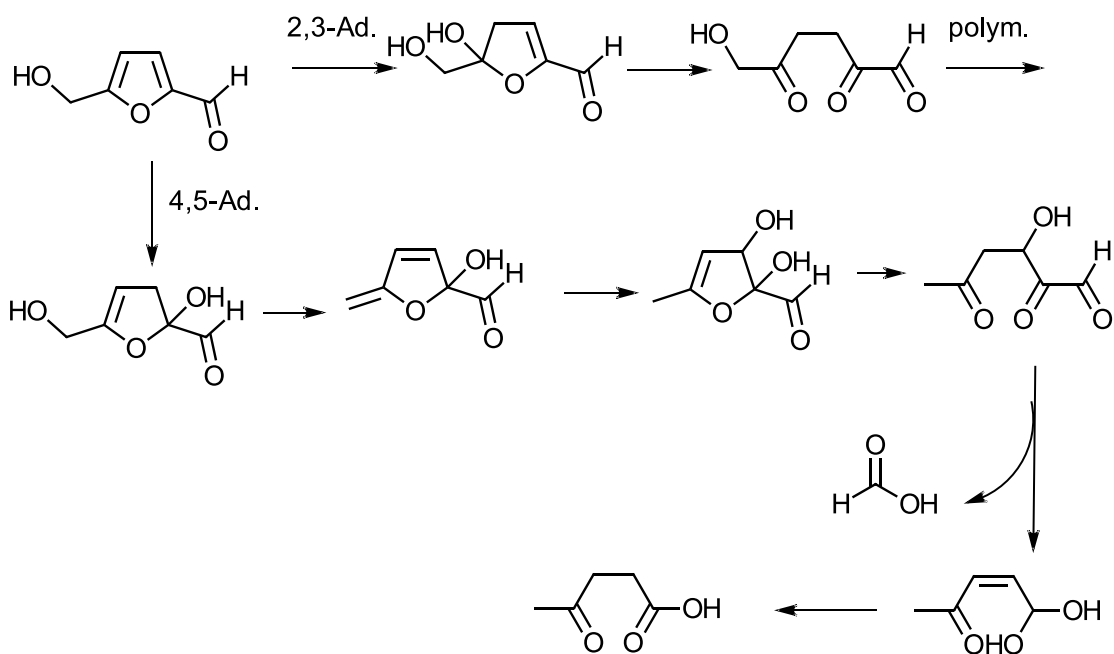


Figure 1.3: Humin formation scheme proposed by Horvat [17] in which a water adds to the alkene adjacent to alkoxy and forms DHH.

Although there is no suggestion as to the polymerization mechanism, this was an important first step in providing a fundamental understanding for how humins

form. Although significant progress in molecular understanding of humins has been made since this original paper, the field still lacks a fundamental mechanistic understanding that is necessary to close this problem.

Horvat's work utilized nuclear magnetic resonance (NMR) solely, in which he was able to identify some of the species present in the reaction [17]. Much of the recent literature has focused on attempting to combine NMR and vibrational spectroscopy, such as Fourier Transform Infrared Spectroscopy (FTIR), to deduce the characteristics of the humin molecular structure [18-21]. The results of these studies are discussed in more detail in Section 1.2.

1.2 Previous Literature

Over the past several years, there have been several speculative structures proposed by the groups of Weckhuysen [18], Lund [19, 20], and Sumerskii [21]. Although Horvat [17] was one of the first to study humins, he only went so far as to propose a precursor to humins, and never the humins themselves. Recent proposals involve a suggested mechanism for humin formation that lead to significantly different linkages and final structures. It's been proposed that the mechanisms could involve nucleophilic attack of α and β carbons on HMF by all other possible good nucleophiles [18], the aldol addition of 2,5-dioxo-6-hydroxyhexanal (DHH) to HMF [19, 20], and the electrophilic attack of the aldehyde carbon of HMF by the alcohol group of another HMF to create hemiacetal and acetal bonds [21], respectively. Although the following structures show examples of the linkages suggested by experimental results gathered by each team above, they are not complete pictures of the polymeric type structure.

1.2.1 Electrophilic attack of HMF

Although the article by Horvat [17] suggests that DHH must be involved in the polymerization reaction to form humins, the first recent attempt to explain humin formation assumed this was not a necessary step [21]. Instead, the group of Sumerskii proposed an electrophilic addition of the aldehyde carbon to the alcohol of another HMF [21] to form acetal and hemiacetal bonds as creating the humin polymer. The mechanism for this process, catalyzed by a Brønsted acid, is shown in Figure 1.4.

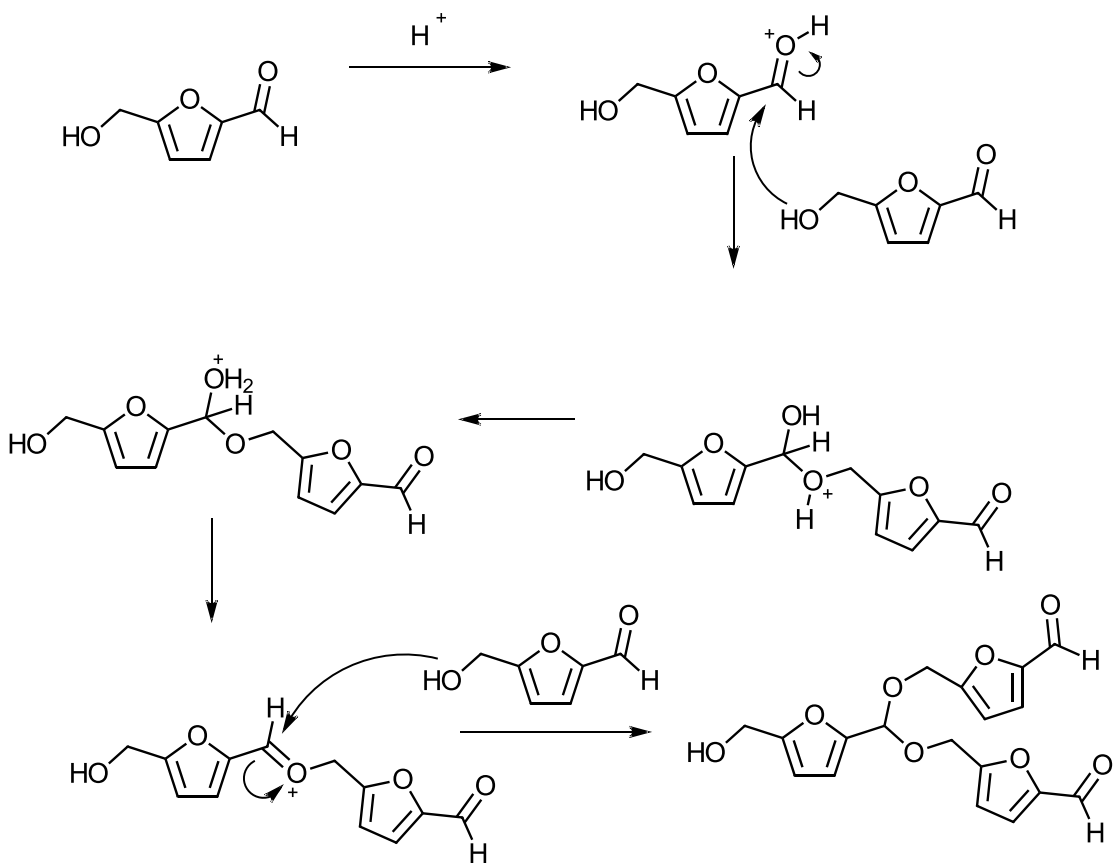


Figure 1.4: Mechanism for electrophilic addition to aldehyde carbon suggested by Sumerskii et al.

The final product from this reaction is the acetal compound that Sumerskii proposes as the basic humin structure, shown in Figure 1.5, below. There are four fundamental vibrational modes of the acetal group, all of which appear in the IR spectrum between 1200 cm^{-1} and 1030 cm^{-1} . These bands appear distinctly in the IR spectrum, and are easily discernible when performing a qualitative analysis [22].

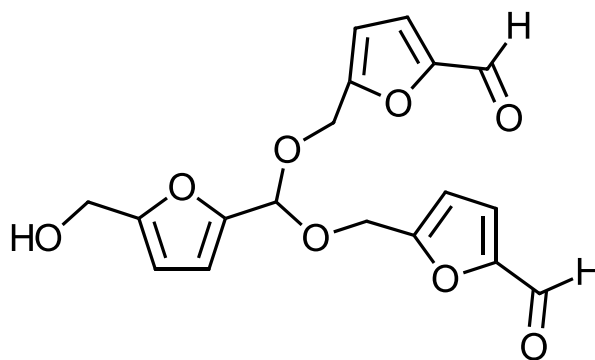


Figure 1.5: Acetal structure proposed by Sumerskii et al. as being the linkages that form humins.

These compounds are significantly different from the others proposed in this section, and should be easily discernible using IR spectroscopic techniques. This will be discussed further in Section 3.4.

1.2.2 Aldol addition/condensation of HMF

The next structure was proposed by Lund et al. as a result of FTIR work combined with attempted mechanistic understanding by varying reaction conditions [19, 20]. Unlike the previous mechanism, Lund's mechanism takes into account the proposed inclusion of DHH originally mentioned by Horvat [17]. There are two proposed structures in these articles that are quite similar and only differ

mechanistically. The first is generated if the aldol addition does not slow after each addition to DHH, and thus results in no further enols on the structure generated. The second is formed when the second addition step is much slower than the first; which gives enols even after all the DHH has been consumed. These structures are shown in Figure 1.6 and Figure 1.7, respectively.

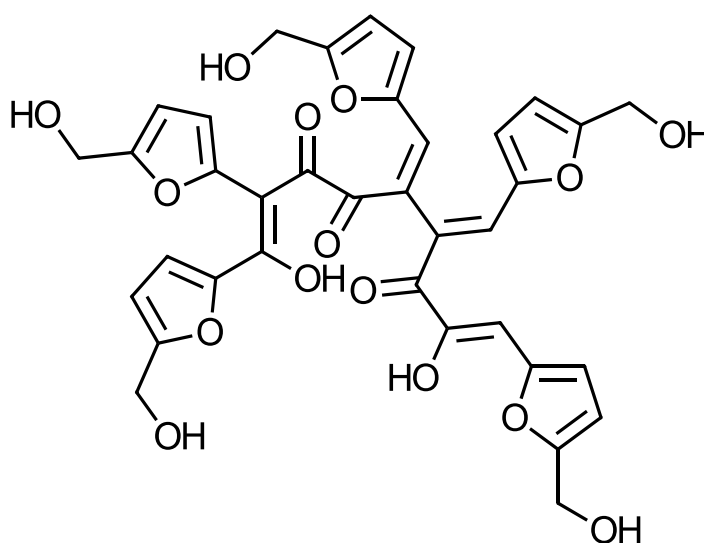


Figure 1.6: Structure proposed by Lund for aldol addition of HMF to DHH where each addition is just as fast as the first.

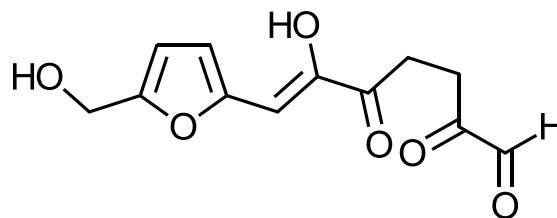


Figure 1.7: Structure proposed by Lund for aldol addition of HMF to DHH where the second addition is much slower than the first.

One of the key features of these structures is that DHH must be present in the reaction mixture, as suggested by Horvat [17]. Although DHH was suggested to be present, it has never been confirmed in reaction mixtures. The formation of DHH is caused by the 2,3 acid catalyzed addition of water, as opposed to the 4,5 addition which leads to levulinic acid, another important intermediate in the process.

Although DHH has never been confirmed as taking place in the reaction, it is highly likely. We tested the likelihood by attempting to form humins with only HMF and formic acid or HMF and levulinic acid. Neither solution formed insoluble particles, suggesting that there must be another species at play.

The suggested mechanism for the process of forming DHH and adding a single HMF via aldol addition is shown in Figure 1.8. The proposed mechanism is based on the work of Horvat [17] and the well-known aldol condensation mechanism that can be found in many organic chemistry textbooks.

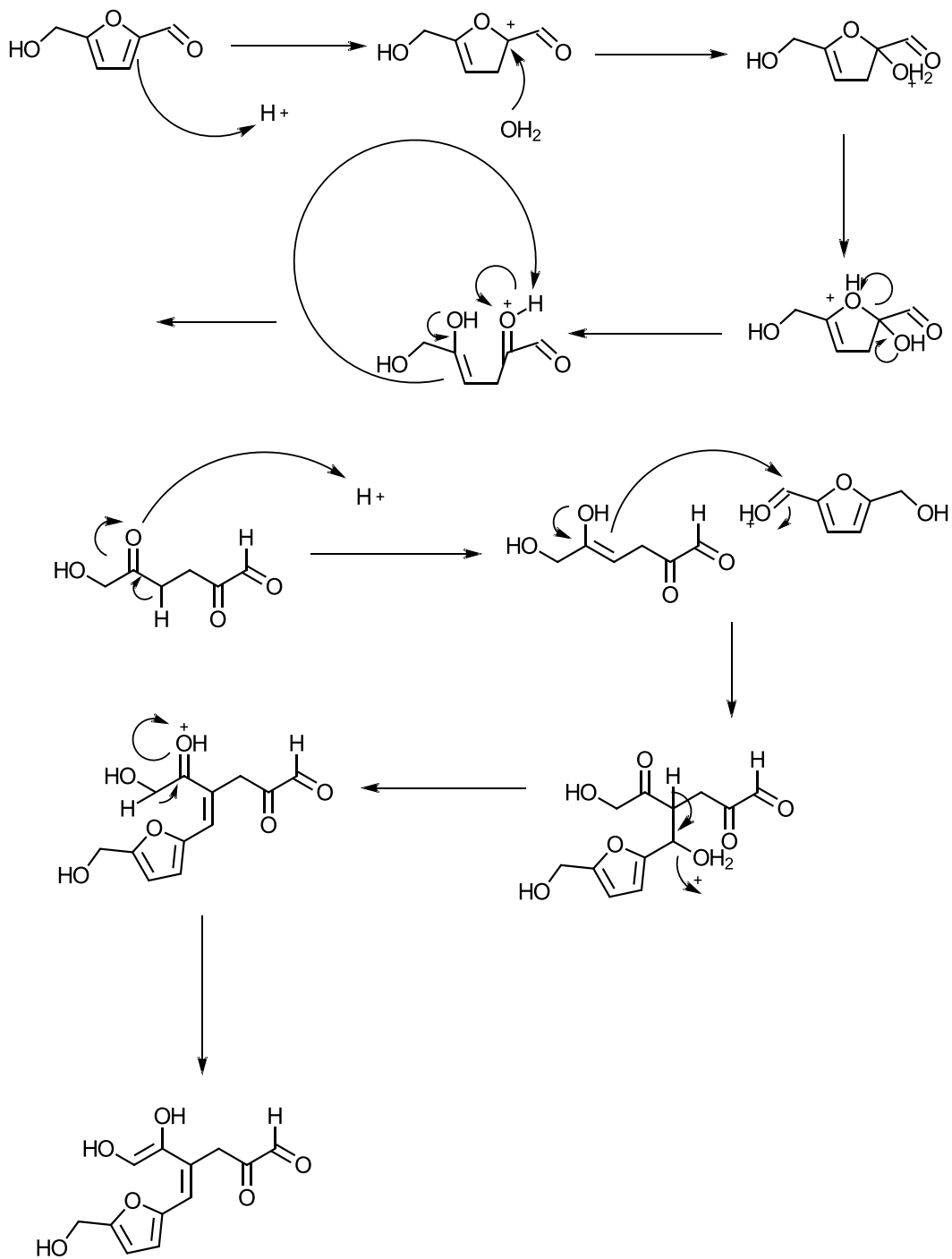


Figure 1.8: Suggested mechanism detailing the formation of a molecule of DHH and aldol addition of a single HMF molecule to it.

1.2.3 Nucleophilic attack on α and β furanolic positions

The most recently suggested structure is that of Weckhuysen et al. and shows the most complex structure. In the article, the group suggests that a combination of formic acid, levulinic acid, DHH, and HMF undergo nucleophilic addition to the α and β carbons on HMF, which result in the structure shown in Figure 1.9. This structure is the most complicated of the four that are considered in this section. This structure was proposed based on extensive work combining FTIR and both solid state and standard NMR results, but there is a lack of focus on the mechanism compared to others [18].

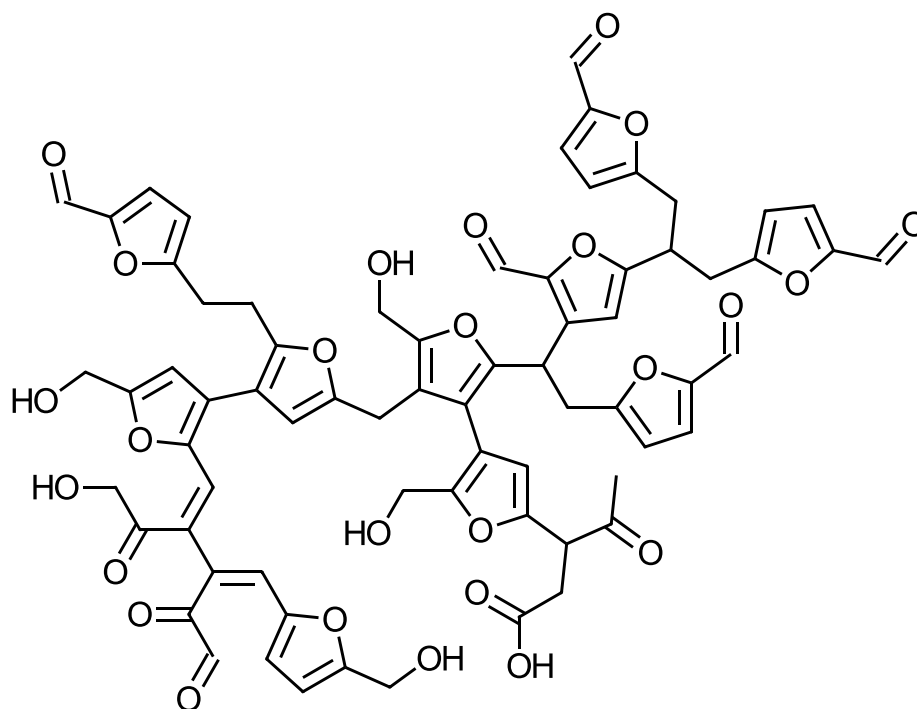


Figure 1.9: The structure for humins resulting from nucleophilic attack of α and β carbons of HMF by all other compounds present in reaction mixture.

1.3 Structure of Thesis

This thesis consists of five chapters. The first will focus on the overview of the field so far, the motivation for this study, and the questions that I hope to answer. The second chapter discusses the experimental methods that were utilized in the approach. Any analytical approaches are also outlined in this section. The third chapter presents the findings of improved knowledge of the molecular structure of humins. In addition, a comparison between our experimental data and literature is made. The fourth chapter outlines the novel technique of studying the growth rate of humin formation by use of *in situ* dynamic light scattering. The fifth and final chapter summarizes our findings for the work and presents any areas that we believe are still open for study.

1.4 Motivation

Humin formation can cause a large problem in plant design. If humins get formed during the dehydration of fructose to HMF, they can get trapped in the reactor drastically increasing the pressure drop across the reactor. This increase could cause equipment failure in upstream pumps or compressors, or it could significantly increase the energy costs for the process. At the same time, with enough formation of humins, they could get carried from the reactor, downstream to pipes and pumps causing scouring problems and damage to equipment. Lastly, humin formation could negatively affect the activity of the catalyst being used in the reactor, which may drastically increase process costs.

In addition to the issues with the overall process economics, humin production limits the selectivity and yield to HMF. Because of this, humin formation is not desired during the biorefining process. When this is taken into consideration, there are

two clear choices as an approach to bringing the economics back closer to an expected value. The first approach to optimize these economics is to hinder the formation of humins. This is a similar approach to attempting to stabilize the HMF under reaction conditions by using a biphasic system [14], or making a careful choice of reaction solvent [15]. The other approach is more accepting of humin formation, but attempts to add value to the structure. This can be accomplished more easily with better understanding of the molecular structure. If the humins can be functionalized for use as a catalyst, acid, adsorbent, etc. the revenue from the process could be greatly increased. Both of these approaches will improve the return on any investment made into the biorefining process. As such, these provide the long term goals for this project.

1.5 Goals of Thesis Work

The goals of this work can be divided into two subsections that directly parallel the motivation for this work: understanding of molecular structure and successfully predicting the growth rate of humin particles.

1.5.1 Understanding Molecular Structure

In order to achieve the long term goals outlined in the previous section, perhaps the most important aspect of a study into humins is gaining an understanding of the molecular structure of the humins as they form. Structural understanding is the basis for predictive and descriptive theories (e.g. phase equilibrium, molecular orbitals, etc.) of chemical species. Knowledge of a compound's structure and the ability to accurately predict its behavior can lead to methods that hinder formation. Secondly, understanding of electronic structure can lead to the ability to predict

reactivity through DFT and other similar calculations. These two features make understanding the structure of the humins of paramount importance. In this study, I will be utilizing vibrational spectroscopic, specifically Fourier Transform Infrared Spectroscopy (FTIR), techniques to deduce structural characteristics of the humins.

1.5.2 Predicting Growth Rate

One of the issues mentioned in Section 1.4 is the insoluble nature of humins in the reaction medium. Because of this, solid waste will build up, causing a drop in catalyst activity and reactor productivity because of increased down time.

Understanding how these insoluble particles form could help the rational design of reactors by examining additional reaction pathways. One way to deal with solid waste is to add filters that can be cleaned easily, to remove the particles as they form.

Understanding where in the reactor these filters are needed is crucial if the filters are to be effective. In addition, catalysts can be designed so that they adequately shed any waste particles before pores become blocked. Lastly, it is important to understand the growth rate of these waste particles so that products don't become contaminated with saturated or unsaturated humins that will nucleate under suitable conditions and cause larger problems downstream (e.g., in an internal combustion engine). In this study, I seek to correlate different reaction conditions with the rate of particle formation to be able to understand the kinetics of this process and influence of temperature, pH, and solvent.

Chapter 2

EXPERIMENTAL DESIGN

2.1 Materials

Reactions were conducted using chemicals purchased in their purest form from Sigma Aldrich. This includes >99% 5-hydroxymethylfurfural, >99% D-(-)-fructose, and >99% D-(+)-glucose. Buffers were prepared using the recipe presented in Appendix A. The actual pH of each system was measured and found to be within 0.03 pH units of the reported value. Reported pH values are determined as calculated from the nominal acid concentration, ignoring activity effects.

2.2 Infrared Spectroscopy (IR)

Spectra for this work were collected with a Nicolet 8700 FTIR spectrometer equipped with a DTG detector and a Golden Gate single-reflection diamond ATR. Using the ATR, spectra were collected from 4000 cm^{-1} to 400 cm^{-1} . Spectra marked as standard resolution (SR) were collected with a resolution of 4 cm^{-1} , by obtaining 16 scans, and the aperture set to 150. Spectra marked as high resolution (HR) were collected with a resolution of 4 cm^{-1} , by collecting 32 scans, with an aperture setting of 100. The optical velocity was 0.1581 with an instrument gain of 8 for both settings.

2.2.1 Normalization of Spectra

In order to increase the specificity, with which qualitative comparisons between spectra could be made for any collected samples, the spectra were

normalized. Hereafter we mention which peak was used to normalize the spectra. For this normalization the Origin 9.1 software was utilized. The normalization was made over a peak where the shape of the peak for the species being compared did not seem to vary. Once the peak had been located, the location of the local minima near the peak was determined. The higher wavenumber minimum was then shifted so that all the spectra crossed the horizontal axis at this location. The peak was then integrated from one minimum to the other, using a straight line connecting the minima as the baseline for the integration. Once the area of the peak had been obtained, the normalized absorbance was obtained by dividing the original absorbance by the area.

2.3 Dynamic Light Scattering

The dynamic light scattering measurements were made using a 389 mW, 532 nm solid state laser from CNI Optoelectronics Technology Co., Ltd. Scattering was collected at 90° using a BI-200SM goniometer from Brookhaven Instruments, Inc. The detector used was a Brookhaven Instruments, Inc. BI-APD. The computer collecting data used the BI-9000AT digital correlator, also from Brookhaven Instruments, Inc. A heating jacket was used to control the temperature of the sample. Samples were prepared in 20 mL scintillation vials and mixed until there was a homogeneous solution present. The acid solvent was prepared by diluting concentrated hydrochloric acid solution. The solution was then filtered, using a 0.2 µm filter, into a 10 mL Wheaton glass reactor vial without a stir bar present. The vial was sealed with a crimped septum top. This was then inserted into the laser apparatus to ensure there were no particles present initially. Once it was verified that the initial solution had no particles, the reaction was started and data was collected in 10 minute intervals.

2.4 High Performance Liquid Chromatography

Analysis of liquids was performed with HPLC, using an Innowax HPX-87H column, held at 50°C. The eluent was 0.005M H₂SO₄, at a flow rate of 0.5 mL/min. A refractive index detector at 35°C was used to measure components in the eluent.

Calculation of any reaction conversions, yields, or selectivities are made using the results of the HPLC analysis. For the purpose of this report, we use the following definitions:

$$y_i = \frac{w_i}{w_{SM}^o}$$
$$s_i = \frac{w_i}{w_{SM}^o - w_{SM}}$$
$$\chi = \frac{w_{SM}^o - w_{SM}}{w_{SM}^o}$$

where y_i is the yield of product i , s_i is the selectivity of product i , χ is the conversion of the starting reactant, SM indicates the reaction starting material, w_i is the mass fraction of species i , and w_{SM}^o indicates the initial mass fraction of starting material in solution.

The calibration curves used for the HPLC are shown in Appendix B. Calibrations were measured using analytical glassware. Calibration samples were prepared with a known mass fraction and molar concentration of analyte. The calibrations were then built by providing the peak area as a function of either molar concentration or mass fraction, as needed. Samples were diluted to remain in the range of the calibration curve, 0.1 wt% - 3 wt%.

2.5 Preparation Procedure

Two steps were needed to produce the humins for analysis. The first step was to perform the reaction to form the humins and the second step was washing the

humins to prepare for analysis. The importance of each of these steps is discussed in their respective sections. The entire procedure is outlined in Figure 2.1.

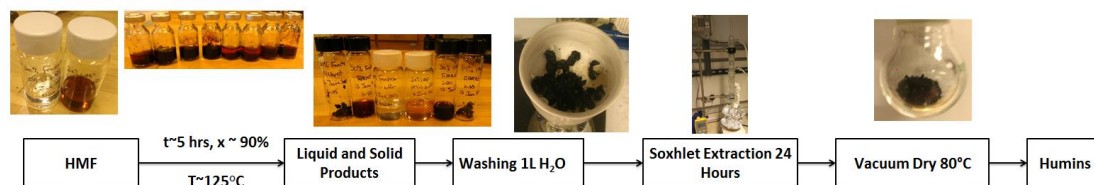


Figure 2.1: Procedure followed for humin production and characterization.

2.5.1 Batch Reactors

10 mL Wheaton glass vials with a small magnetic stir bar were sealed with a crimped top. The vials were added to an aluminum reaction block. The temperature for the reactions was 125°C , as measured by thermocouples inserted into the oil that was in a well adjacent to the last reaction vial. The solvent used for the reaction was a HCl/KCl buffer system, whose recipe is described in Appendix A. The reactions took place for more than 5 hours, in order to achieve a high yield of humins. Desired conversion of the starting material was $> 90\%$, as measured by HPLC.

2.5.2 Washing Humins

Once the humins had been formed during reaction, they needed to be prepared for analysis. The humins needed to be washed because it was determined that there were products of reaction adsorbed on the humin material itself. This led to concern that any characterization would be affected by the species adsorbed on the humin, and not the humin itself.

Chapter 3

STRUCTURAL IMPLICATIONS OF VIBRATIONAL SPECTROSCOPY MEASUREMENTS

3.1 Basics of Vibrational Spectroscopy

The physical background for vibrational spectroscopy is discussed in Appendix C. For the purposes of this thesis, all the necessary information is presented in the body. When a molecule is struck by a photon of light, it absorbs the energy as long as it can store the light energy in some way. For IR light, this storage mechanism is the vibration of the molecule. Each compound has a specific absorption spectrum that can be used to determine the structure of the compound. When the light is absorbed, the molecule changes its vibrational state in a characteristic way, called a vibrational mode. The number of vibrational modes that a molecule contains is related to the number of atoms contained in the molecule and the symmetry components of the molecule. For nonlinear molecules this leads to $3n - 6$ degrees of freedom while linear molecules have one less degree of freedom. When the absorption spectrum is plotted, functional groups of the molecule have general energies that they absorb at, which can be utilized to determine the functionality of a molecule. In order for the vibrational mode to be IR active, the vibration must change the dipole moment of the molecule. The frequency of the vibration, and of the absorbed light, is related to the strength of the bond that is vibrating and the reduced mass of the bonded atoms.

$$\bar{\nu} = \frac{1}{2\pi c} \sqrt{\frac{k}{\mu}}$$

$$\mu = \frac{m_1 m_2}{m_1 + m_2}$$

An example table for the carbonyl functional group is shown in Table 3.1, but the rest of the functional group tables used in this study are shown in Appendix D.

Table 3.1: Example characteristic vibrations for the carbonyl functional group.

Group	Frequency (cm ⁻¹)	Comments
-CH ₂ -C(=O)-CH ₂ -	1725 – 1700 [22, 23]	Strong intensity
-CH=CH-C(=O)-CH ₂ -	1695-1660 [22, 23]	Additional band of C=C shows 1650 – 1600 cm ⁻¹
Ar-C(=O)-CH ₂ -	1700-1680 [22, 23]	
-CH=CH-C(=O)-CH=CH-	1665 [23]	
-CH=CH-CH=CH-C(=O)-CH ₂ -		
Ar-C(=O)-Ar		
7-member C(=O)	1705 [23]	
6-member C(=O)	1715 [23]	
5-member C(=O)	1745 [23]	
4-member C(=O)	1780 [23]	
3-member C(=O)	1850 [23]	
-CH ₂ -C(=O)-H	1740 – 1720 [22, 23]	2850 – 2820, 2750 – 2720 band due to Fermi resonance of δC-H and νC-H
-CH ₂ -C(=O)-OH	1760-1700 [22, 23]	Much stronger intensity than the ketone carbonyl

These tables can be combined to make a complete mapping of the spectral space to be able to predict where bands might appear. For this study, we focused on any bands that contained carbon, oxygen, and hydrogen atoms, and ignored the other heteroatom containing groups.

3.2 Establishment of Humin Processing Protocol

The concerns initially raised in Section 2.5 were validated when the humins were first washed. The pH of the wash water was measured at each 10 mL fraction

that was collected. It is clear that after an excess of water was used, the pH began to have increased scatter, as shown in Figure 3.1. After this, it was suggested to use a large excess of water in the procedure in order to guarantee the acids on the humins were removed.

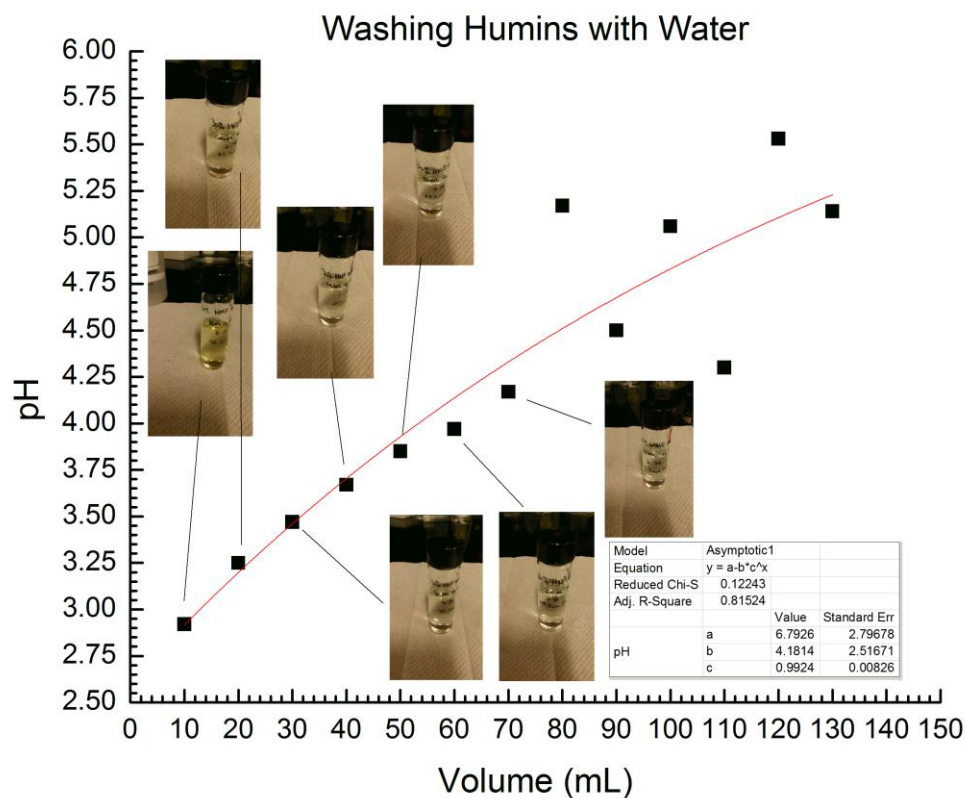


Figure 3.1: pH of aqueous wash versus volume used during the washing procedure.

When the wash liquid was analyzed by means of HPLC, it was also determined that levulinic acid and formic acid were both present in very low concentrations. These species absorb strongly in the carbonyl region of the infrared spectrum, and

were found to overlap with the humin spectrum. In order to accurately characterize the humins, these species need to be removed from the humins by washing.

The effect of the washing on the structure that was deduced from infrared spectroscopy was analyzed extensively. The infrared spectra that were measured during these experiments are shown in Figure 3.2.

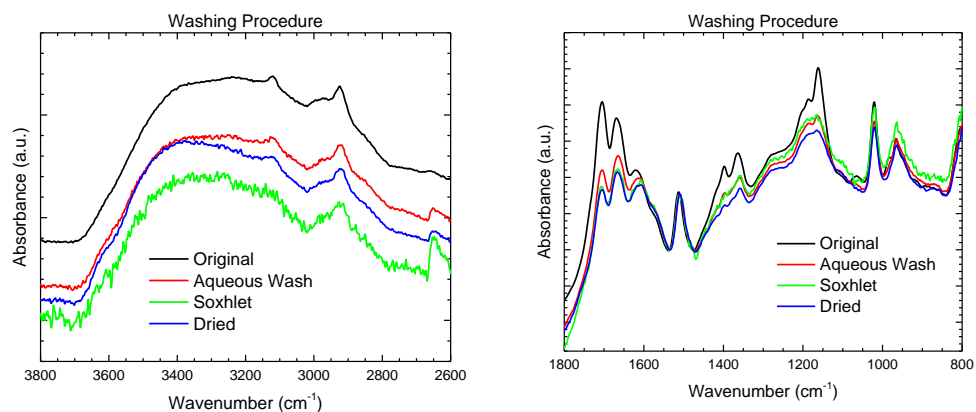


Figure 3.2: Effect of washing humins on the SR - IR spectrum in the region of 2600-3800 wavenumbers (a), and 800-1800 wavenumbers (b). The spectra are normalized to the peak at 1500 cm⁻¹.

The normalization for the above spectra was performed on the peak at 1500 cm⁻¹. Normally, we tried to use the peak at 1200 cm⁻¹ which fits the backbone of the humins. The reason we could not use that peak in this case is that the levulinic acid

originally present in the humins has a sharp peak that overlaps with this peak, and would distort the normalization.

One region of great interest is the C=C and C=O stretching region typically found from 1500 cm^{-1} – 1750 cm^{-1} . In this region, there are 4 bands that can be observed. However, it is important to note that there are more than these four features that overlap and are convoluted to cause the resulting spectrum. The large number of bands contributing to the spectrum in this region suggest that there are many different types of C=C and C=O bonds (e.g., varying strength and length). However, this region can be very helpful because there are many C=C and C=O structures present in HMF, DHH, formic acid, and levulinic acid, which will all be present in the reaction mixture. The peak at 1500 cm^{-1} is due to the “breathing” of the furan ring, and is also present in pure HMF.

There is not much of a difference between the spectra shown in Figure 3.2 (a), while there are significant differences seen in the spectra presented in Figure 3.2 (b). However, in Figure 3.2 (a) it is interesting to note that the position of maximum absorbance in the O-H band appears to shift to higher wavenumbers. This could be ascribed to the removal of water, which decreases the interference of water with the alcohols in the humin itself. In the region shown in (b), it is clear that the original humins have many differences from the humins after they are washed and dried. Some important aspects to note are the disappearance of the shoulder on the band at 1708 cm^{-1} , and a marked decrease in the intensity of the carbonyl bands at 1708 cm^{-1} and 1666 cm^{-1} . These bands are largely due to the levulinic acid and HMF absorbed on the humins, but the formic acid contributes a broad band centered around the 1650 cm^{-1} region. We also observe the removal of the sharp peak present at 1150 cm^{-1} that is

caused by levulinic acid. In addition, there is a small peak present at 1066 cm^{-1} that is no longer present after washing. At this point, it is suspected that the removal of adsorbed HMF, fructose, levulinic acid and formic acid cause the change in the spectrum. This hypothesis was further strengthened by HPLC analysis of the wash liquids, which showed small amounts of all of the above species.

The IR spectrum of humins, HMF, levulinic acid, and formic acid were also compared to see which one contributed to the humin structure. The comparison for the low wavenumber region, shown in Figure 3.3, clearly shows that the humin structure has many of the characteristics of the HMF and levulinic acid. For example, it is clear that the carbonyl of the levulinic acid also appears in the same vibrational frequency of the humins. In addition, there appears to be the same furan peak that is present in HMF at 1510 cm^{-1} that is slightly red shifted in the humins. This would be caused by decreasing the strength of the ring, which would arise from changing the substituents on the furan ring. As this is likely in the formation of humins, it seems reasonable that we observe a shift in the furan breathing mode at 1500 cm^{-1} .

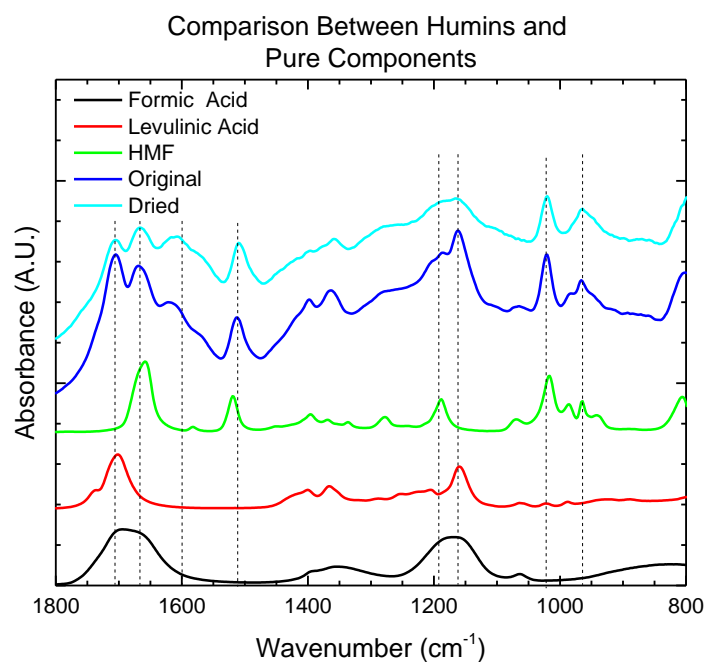


Figure 3.3: Comparison of humins before and after washing with the starting materials and products of reaction (HMF, levulinic acid, formic acid). SR humin spectra are normalized to 1500 cm⁻¹ peak, while starting material structure is normalized to get similar peak heights.

3.3 IR Spectra

After completing the requisite washing procedure, the humin's infrared spectrum was recorded. The spectra were normalized with the Origin software as described in Section 2.2.1. By this normalization, it is possible to make improved qualitative distinctions between the spectra that were collected. As there was no internal standard used during the measurement, and the path length for each measurement varied, it is impossible to make quantitative measurements from this study.

3.3.1 ATR-FTIR of Humins and Vibrational Assignments

Figure 3.4 shows the FTIR spectrum of humins prepared from HMF as a reactant. By using the tables in Appendix D, the peaks observed in the IR spectrum can be assigned to the vibrational (stretching, rocking, wagging, etc.) movement of atoms inside a molecule. By analyzing the high frequency region (above 3000 cm^{-1}), the characteristic broad band due to hydroxyl groups located at 3400 cm^{-1} can be clearly observed. The width of this band is larger than any other band in the humin's spectrum and reflects the wide distribution of different strengths of OH groups. OH groups that do not participate in hydrogen bonding, "free OH", are expected at wavenumbers on the high end of this band. OH bonds that are a part of an acid group are expected at lower wavenumbers. We also see both the saturated and unsaturated C-H stretching vibrations that are expected. The saturated C-H stretches appear at 2920 cm^{-1} . The unsaturated stretch is solely due to alkene C-H stretching, and appears at 3130 cm^{-1} . These stretching modes are present in most organic compounds, but the presence of the unsaturated stretching mode is necessary if the presence of alkene groups are suspected. The lowest wavenumber C-H stretch that is expected is that of an aldehyde group, but the intensity of any aldehyde peaks that might be present is too low to be easily discernable in these spectra.

In addition, we can see that there are several peaks in the region of 1500 cm^{-1} to 1800 cm^{-1} . These peaks can be assigned to carbonyls, conjugated carbonyls, alkenes, and aromatic alkenes in order of decreasing wavenumber. This type of spectrum would appear if HMF was incorporated in the backbone of the polymer structure.

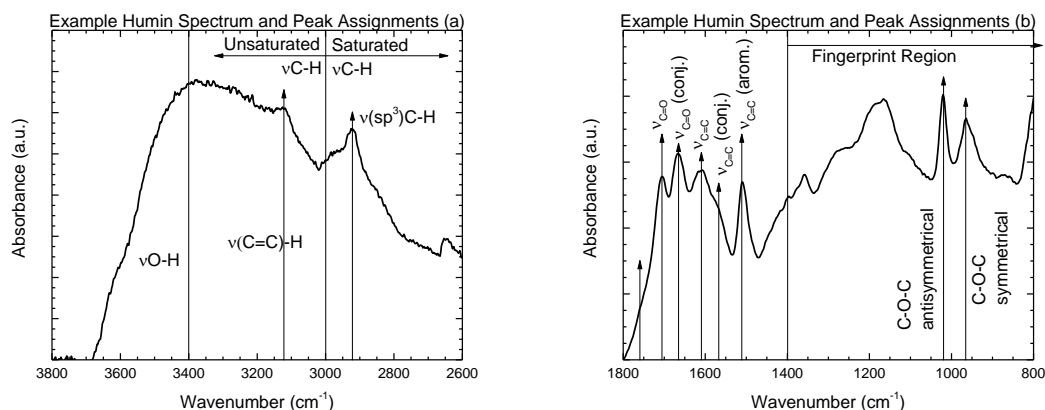


Figure 3.4: Example spectrum of 30% HMF humins in pH 1.1 buffer. Certain spectral characteristics are noted because of their importance in deducing structures of the humins.

3.3.2 Effect of Starting Material on Humins' Structure

Together, the groups of both Lund [19, 20] and Weckhuysen [18] have shown that there are no significant differences between humins formed from fructose, glucose, and HMF. However, our spectroscopic analysis has shown multiple peaks that present differences in the spectra. We believe this difference arises from performing a rigorous washing procedure including the Soxhlet extraction, whereas Lund did not follow such a procedure. Weckhuysen, who performed a rigorous washing procedure, did not examine any humins formed directly from HMF. We provide the spectra that we collected for the comparison in Figure 3.5. We speculate that the peak at 1650 cm^{-1} is due to the interactions of HMF, because it is only present when the concentration of HMF is initially large. We also see the furan stretching mode at 1500 cm^{-1} indicating that all of the humins must form through some furanic compound. Lastly, in glucose, it appears as if there are many peaks that make up the

background of the spectrum that still need to be fit. The shape for the glucose and fructose spectra are very similar, but the glucose peak at 1600 cm^{-1} appears much broader than the same peak in the fructose and HMF humins. The glucose and fructose humins show the most similarities in the $1500 - 1700\text{ cm}^{-1}$ region, while the HMF and fructose humins show the most similarities in the $1100 - 1300\text{ cm}^{-1}$ region.

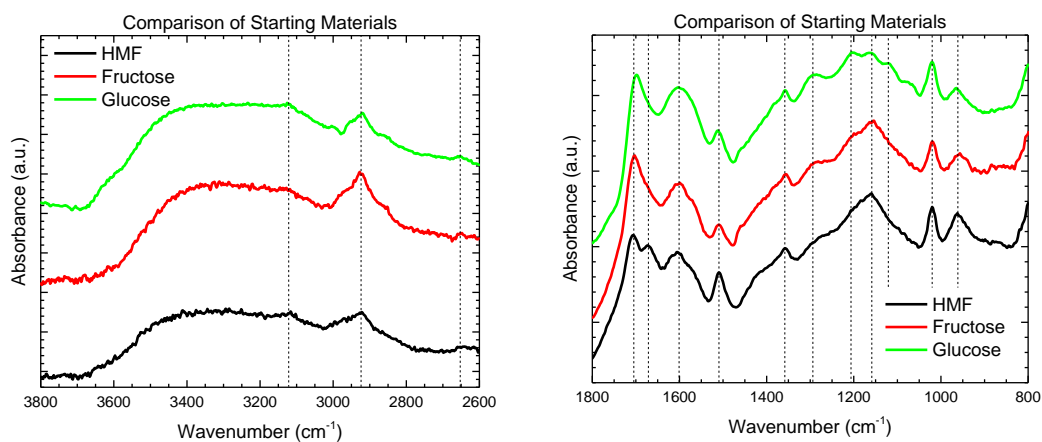


Figure 3.5: Effect of sugar on humin structure. Spectra show that both humin samples are significantly different, most notably in the $1600\text{-}1700\text{ cm}^{-1}$ region.

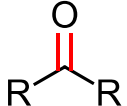
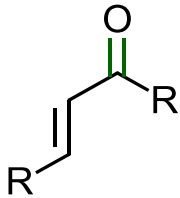
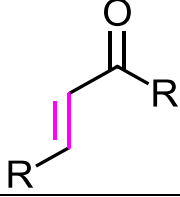
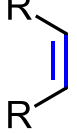
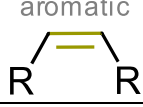
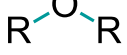
The high frequency region of the humin spectra shows very similar characteristics for each of the starting materials. There are clearly O-H stretching modes that are centered around 3400 cm^{-1} , a $=\text{C-H}$ stretching mode at 3120 cm^{-1} , and the $\text{sp}^3\text{ C-H}$ stretching mode at 2920 cm^{-1} . Although the peak at 2650 cm^{-1} is less intense, it is still clear that there is an aldehyde $-\text{C-H}$ stretching mode at this frequency. This aldehyde stretching mode is at a much lower frequency than would be

predicted by the tables in Appendix D. This would occur if the strength of the bond was decreased for any reason.

3.4 Validity of Proposed Structures

As the goal of this study was to understand the molecular structure of the humins, it is important to first understand how the structures proposed by Weckhuysen [18], Lund [19, 20], and Sumerskii [21] fit with the experimental data that have been obtained. All of these assignments are made using the tables found in Appendix D. For ease of reading, the results of this section are summarized in Table 3.2.

Table 3.2: Infrared bands observed experimentally, and that should be observed based on the proposed structures of Weckhuysen [18], Lund [19, 20], and Sumerskii [21]

Band	Wavenumber (cm ⁻¹)	Supported by Structure (Yes/No)			
		Weckhuysen	Lund (slow/fast)		Sumerskii
	1700-1710	Yes	Yes	No	No
	1640-1690	Yes	Yes	Yes	Yes
	1570-1580	Yes	Yes	Yes	Yes
	1590-1620	Yes	Yes	Yes	No
aromatic 	1480-1520	Yes	Yes	Yes	Yes
	1000-1050 (symmetric)/ 940-1000 (anti-symmetric)	Yes	Yes	Yes	Yes

The humin structure proposed by Weckhuysen [18], shown in Figure 3.6, is analyzed first. This structure is the most complex of those proposed, and appears to have the most complete description of bands appearing in the experimentally obtained infrared spectra. For example, in this structure there should clearly be several different carbonyl bands because of the different types of conjugation present in the molecule.

In addition, there should be an aldehyde and acid carbonyls present. The only evidence not immediately clear about this molecule is the presence of the aldehyde in the structure. This is not easily observed, but could be confirmed more easily with Raman spectroscopy where the C-H scatters IR light more intensely than it absorbs IR light.

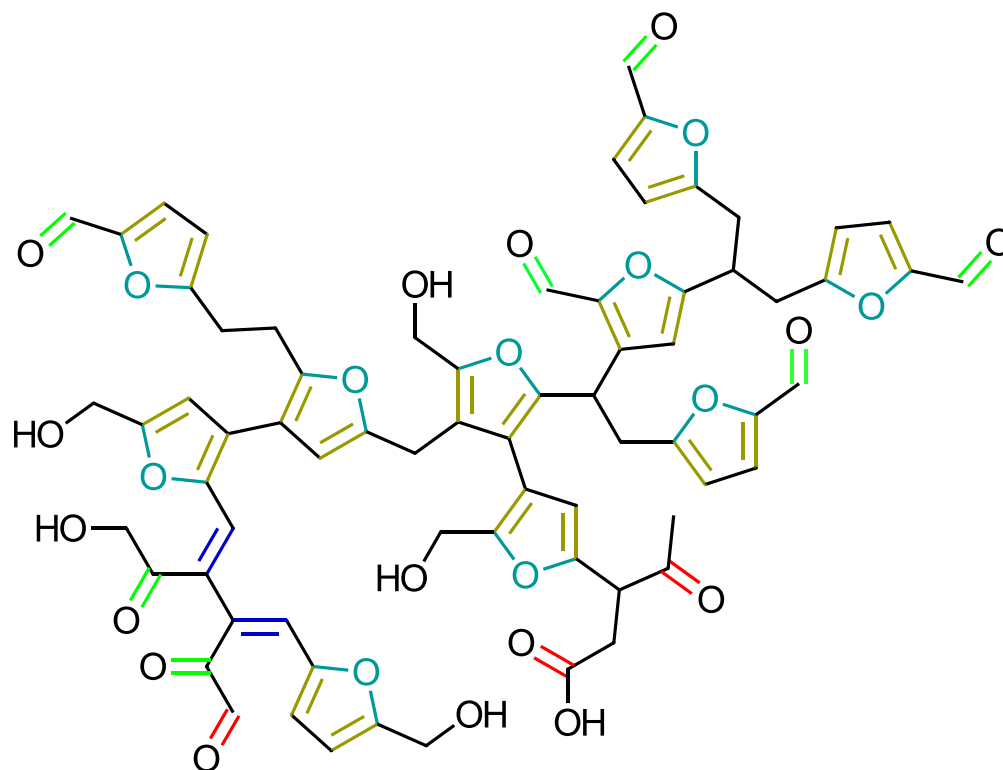


Figure 3.6: Humin structure proposed by Weckhuysen, where bonds are labelled according to the frequency they should have in the infrared spectrum.

The humins shown in Figure 3.7 and Figure 3.8 are those proposed as forming from aldol condensation of HMF and DHH. The first humins are those formed when the addition of a HMF slows the rate of subsequent addition of HMF. The second

humins are those formed when each of the possible 5 additions to DHH has the same rate (i.e., there is no DHH deactivation).

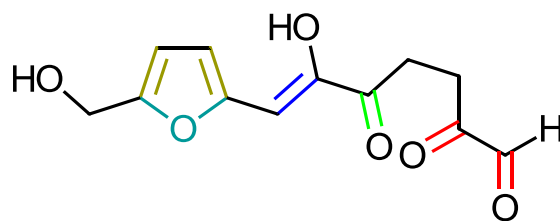


Figure 3.7: Humin structure proposed by Lund when the rate of addition slows down upon each HMF addition.

The next set of humins, shown in Figure 3.8, are similar to the previous, but the reaction rate does not change with each addition. Because of this, there are no more α hydrogens present in the structure to which HMF can be added. The structure again accounts for the infrared characteristics that we observed experimentally, suggesting that this structure could also fit with the observations made. However, this structure does not account for the presence of non-conjugated carbonyl bands, which makes it less likely than the previous two structures for being a good candidate of the humin structure.

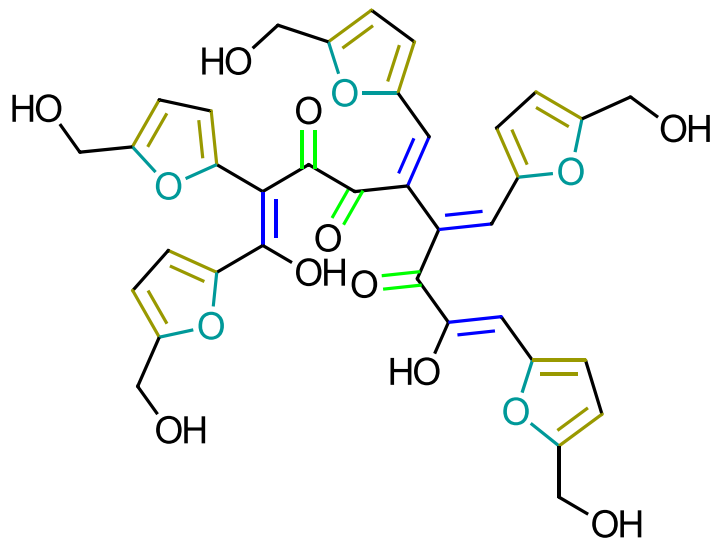


Figure 3.8: Humin structure proposed by Lund when the rate of addition does not change.

Lastly are the humins that are suggested as forming through electrophilic attack, which do not show the non-conjugated carbonyl bonds but instead show distinct acetal bands in the region of $1200 - 1030 \text{ cm}^{-1}$. Because of this, this is the least likely of the proposed structures.

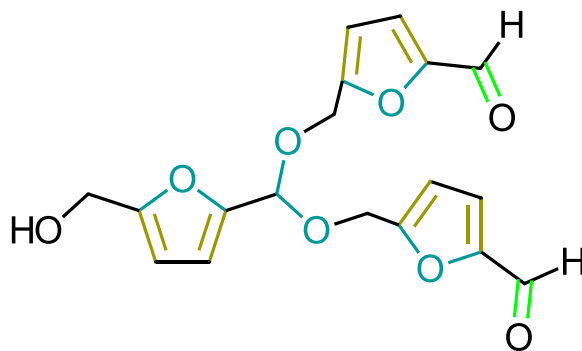


Figure 3.9: Humin structure proposed by Sumerskii.

3.5 Dependence of Humin Structure on Conversion

The structure of the HMF humins was examined as a function of HMF conversion. Three samples of humins were produced at reaction times of 5 hours, 24 hours, and 30 hours. The humin structure shows significant variations in the peak around 1650 cm^{-1} . As this peak was ascribed to HMF present in the humins, the disappearance of this peak fits with our understanding of the kinetics.

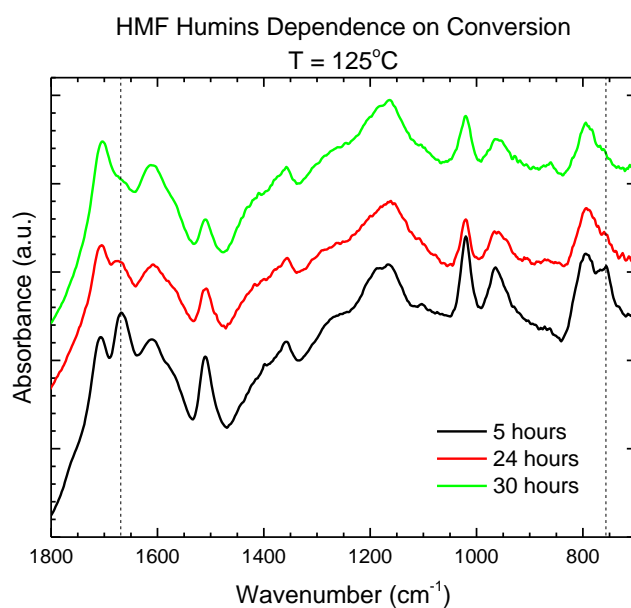


Figure 3.10: Humin structure as a function of conversion at 125°C . Conversion ranges from 90% at 5 hours to 100% at 30 hours.

Using the tables of Appendix D, we can confirm that this peak is likely due to the stretching vibration of a conjugated C=O band. Due to a decrease in the relative intensity of this peak with increasing HMF conversion, we are led to believe that there must be HMF incorporated into the humin structure. This raises the question of where

the HMF is attached in the humins, because the washing should remove any liquid reaction products. We therefore speculate the presence of chemically bound HMF in the humins that can be consumed as the bulk HMF concentration decreases. This fits with the description of the humin structure changing over time, because there is a composition shift during the consumption of HMF bound to the humins.

Figure 3.5 shows that the main difference between humins formed from HMF and from glucose or fructose is the presence of the peak at 1650 cm^{-1} . By comparing these two results, we can speculate that as soon as an HMF is formed from either fructose or glucose, it is converted to humins fairly fast. Since this is such an important observation of this study, much more work needs to be focused on collecting a larger data sample as a function of conversion. In addition, further study on the humin structure as a function of conversion could elucidate the mechanistic differences between different types of humins.

3.6 Conclusions from Molecular Characterization

By utilizing FTIR, we have been able to make the recommendation that of the humins speculated in recent literature, those suggested by Weckhuysen appeared to be the most accurate. This structure also appears to fit well with the humin structure changing as a function of conversion because it incorporates many HMF molecules in the structure. In addition, we show that humins formed from HMF, fructose, and glucose show significant differences in the carbonyl region. These differences were ascribed to the low concentration of HMF present in the fructose and glucose humins. This was further supported by analyzing the humins formed from HMF as a function

of HMF conversion. As conversion increased, the relative intensity of the peak at 1650 cm^{-1} decreased with respect to the peak at 1700 cm^{-1} .

Chapter 4

GROWTH RATE OF HUMIN PARTICLES

4.1 *In Situ* Light Scattering Kinetic Data

The dynamic light scattering experiments were conducted as described in Section 2.3. The goal of this portion of the study was to determine how fast humin particles grow and how the growth rate depends on reaction conditions. The conditions examined are presented in Table 4.1.

Table 4.1: Operating conditions used for the *in situ* DLS studies.

Temperatures (°C):	50, 60, 70
[HCl] (M):	1.00, 0.32, 0.10

Dynamic light scattering can be used to determine the size of particles by determining the diffusivity of the particles in solution. The theoretical background of the experiments is discussed in more detail in Appendix E. At the end of each experiment, the conversion of HMF was measured using HPLC. The results of the HPLC were replicated *ex situ* to confirm the results as they appeared erroneous initially. The HPLC data determined for each of the DLS experiments are presented in Table 4.2 – Table 4.5.

Table 4.2: Conversion of HMF in each of the DLS experiments.

HMF (% Conversion)	pH =	0.0	0.5	1.0
T (°C)=				
50		1.5	2.0	1.7
60		3.1	2.4	3.3
70		10.1	2.6	1.4

Table 4.3: Yield to formic acid from HMF in DLS experiments.

FA (% yield)	pH =	0.0	0.5	1.0
T (°C)=				
50		0.3	0.2	0.1
60		0.8	0.4	0.2
70		2.1	0.7	0.4

Table 4.4: Yield to levulinic acid from HMF in DLS experiments.

LA (% yield)	pH =	0.0	0.5	1.0
T (°C)=				
50		0.4	0.2	0.1
60		1.8	0.8	0.3
70		4.8	1.5	0.7

Table 4.5: Reaction time used in DLS experiments.

Final Time	pH =	0.0	0.5	1.0
T (°C)=	min			
50		90.12	180.02	227.60
60		90.33	150.10	230.08
70		75.42	89.93	160.40

4.2 Autocorrelation Results

The output of the dynamic light scattering experiments is an autocorrelation between the electric field intensity at an initial time and some later time, where the separation between time points is the delay time. An exponential decay in the autocorrelation function indicates particles of a certain size. The shape of the decay influences the shape of the distribution of particle sizes. The autocorrelation functions that were collected for the DLS experiments are presented in Appendix F. An example of the autocorrelation function dependence on reaction time for an arbitrary humin reaction is shown in Figure 4.1.

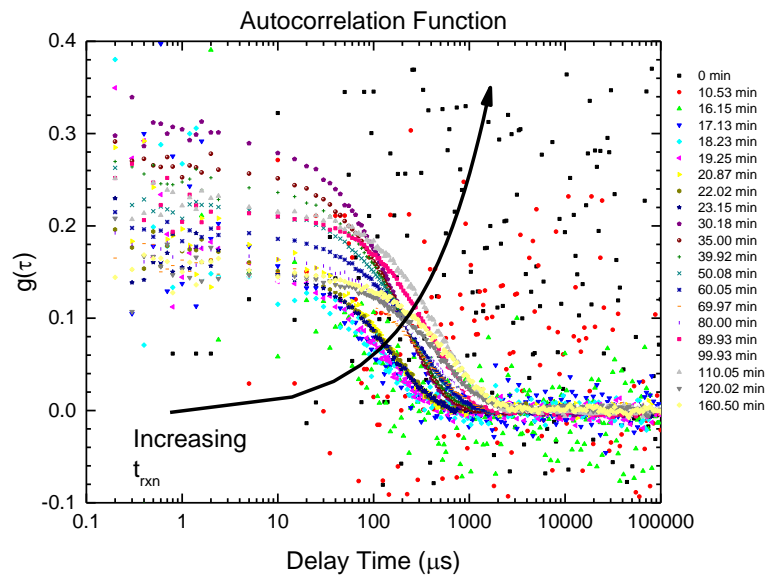


Figure 4.1: Example autocorrelation functions for a typical DLS experiment.

Before the reaction occurs, there are no particles in the mixture, so the autocorrelation function is scattered randomly. This is true even until the induction time for the reaction occurs, and a correlation appears once particles are formed. As

the reaction proceeds, the correlation begins to shift so that the decay occurs at longer and longer delay times. This indicates that the size of the particles is indeed growing over time, assuming that the viscosity of the solution remains constant. In addition to monitoring the autocorrelation function as the reaction progresses, we measure the average intensity of scattered light. In these experiments, the laser power was constant throughout, so a change in the scattered light intensity indicates a change in the particles. If we assume that the Rayleigh theory of light scattering holds, the scattered intensity varies as the particle radius to the sixth power, and proportionally to the number of particles. Before the reaction starts, the average scattered light intensity was consistently 1.9 kcps, but during the reaction an optimal value for recording autocorrelation functions was between 50 kcps and 500 kcps. From this brief analysis, it is clear that to make quantitative measurements with our data, we need an accurate model with which to fit the data.

4.3 Autocorrelation Fit Methods

In order to determine the proper method to fit our data, we needed an idea of the type of distribution of particle sizes. In order to get this, we had to make some observations about the correlation functions we obtained. In an autocorrelation function with a single exponential decay time, there is a monomodal distribution. If there are two exponential decay times, there is a bimodal distribution. Because we saw some samples that contained two decay times, we decided that it would be best to use a fit that could incorporate the bimodal aspects of it. As such, any type of the cumulant fitting models could not be used, but the non-negative least squares (NNLS) or CONTIN methods could still be used for analysis. In the end, the CONTIN method was used for all samples because the residual between the fit and experimental data

seemed to be scattered the most randomly and seemed to have the lowest root mean squared error. Once a fit was made, the Einstein-Stokes relationship, shown in the equation below, was used to relate the particle diffusivity to the diameter of the particle.

$$D = \frac{k_B T}{6\pi\mu r}$$

where D is the particle diffusivity, k_B is the Boltzmann constant, T is the absolute temperature, μ is the solution viscosity, and r is the particle radius. In this case, the diffusivity is measured and the particle radius is calculated directly. The light scattering software that was installed on the instrument had these calculations built in, so most analysis was done with that software.

In order to use the Brookhaven software for analysis of the particle size distribution, the viscosity of the solvent had to be set first. Then the autocorrelation function could be compared to the fit to make sure that the model was producing a valid result. An example of this is shown in Figure 4.2. In this example, a theoretical model is fit to the autocorrelation function, and it shows a relatively clean fit. Two factors were taken into account before using the size generated by a fit. The first factor was the difference in autocorrelation function baseline when measured by a slope analysis, and when measured at extended time delay channels.

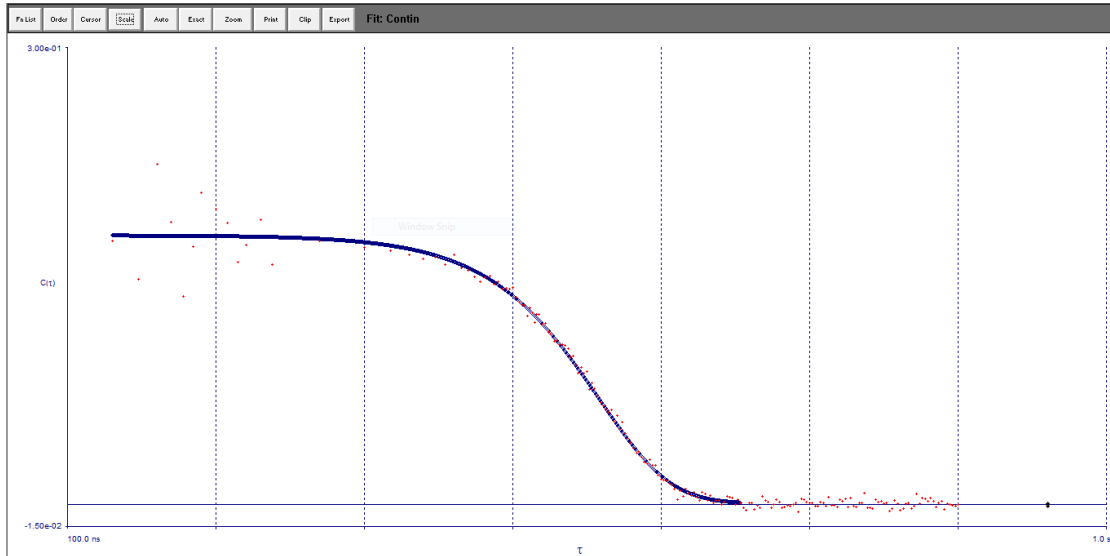


Figure 4.2: Example of using the Brookhaven Instruments software for analysis of the DLS measurements.

An additional example using a bimodal particle distribution can be seen in Figure 4.3. In this case, the distribution consists of much smaller particles that show up at a shorter delay time and another population consisting of larger particles at the longer delay times.

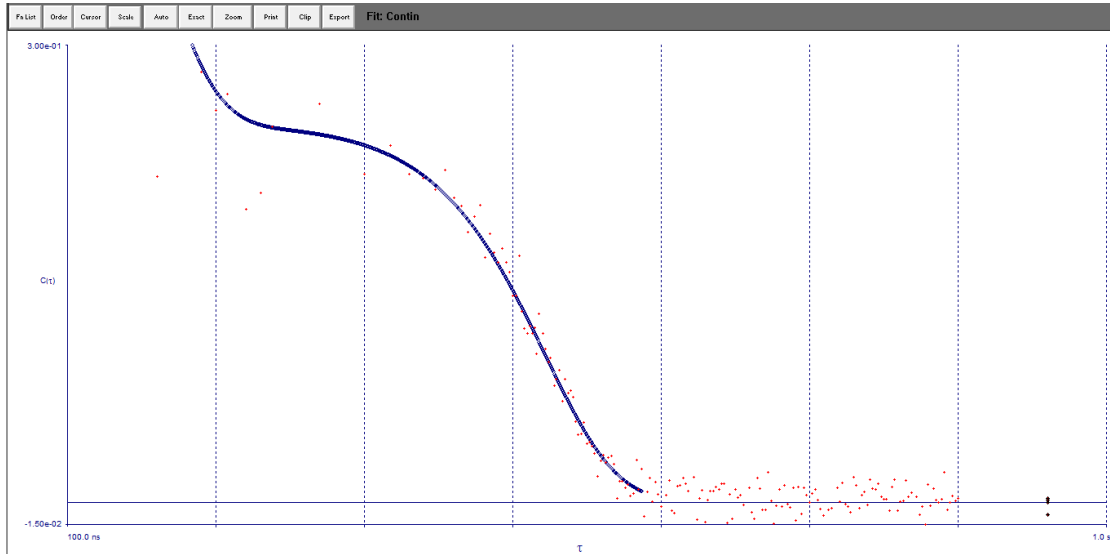


Figure 4.3: Example autocorrelation function with bimodal distribution.

It is also important to determine when the fit produced by the software is acceptable, and when the value needs to be ignored. Figure 4.4 shows an example of this case. In this example, the baseline as measured by the extended delay channels is significantly different from that obtained by calculating using an autoslope analysis. The biggest reason for this discrepancy is that there is not a baseline plateau that is expected in light scattering data. Because of this, the measurement should not be used in any of the analysis. The data was examined for correlation functions that had characteristics like this indicative of bad data. In addition, although the data shown below is clearly bad, the software has tried to fit it. It is clear that the fit is not trustworthy because it does not capture the behavior of the autocorrelation function. For any points included on the plots in the upcoming sections, the autocorrelation functions themselves and the fitted values were checked to make sure these data are accurate. For the majority of the fits, the CONTIN method appeared to model the

behavior of the data the most closely for almost every case. Because of this, the CONTIN fits are the default used, but if the fit is bad, either NNLS or the cumulant cubic method was used.

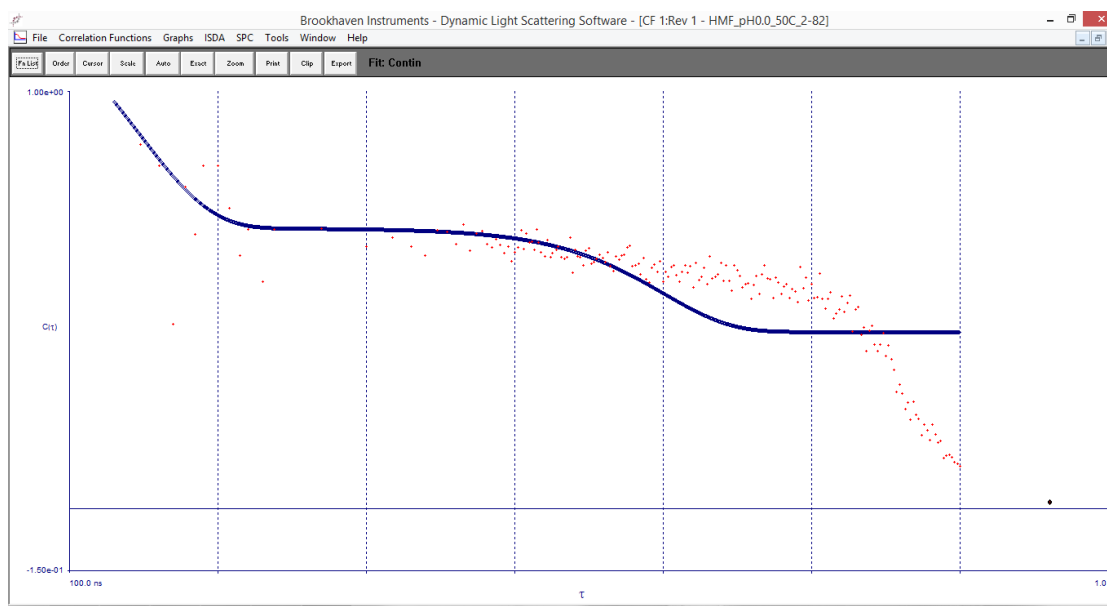


Figure 4.4: Example autocorrelation function where the autocorrelation data is not good and the fit is poor.

When the fit had been confirmed, the software provided a particle size distribution that can be taken and used for kinetic analysis. The particle size distribution for the bimodal example above is shown in Figure 4.5. In this example, the software suggests particle sizes of 0.19 nm and 200 nm. The smaller particles would have to have diameters that are on the order of molecular diameters if this were true. Because of this, it is likely instead that these diameters are just a measurement, or fitting, error. Once the size distribution has been determined, the data is exported for

analysis on the kinetics as a function of reaction conditions, which will be the focus of the next section.

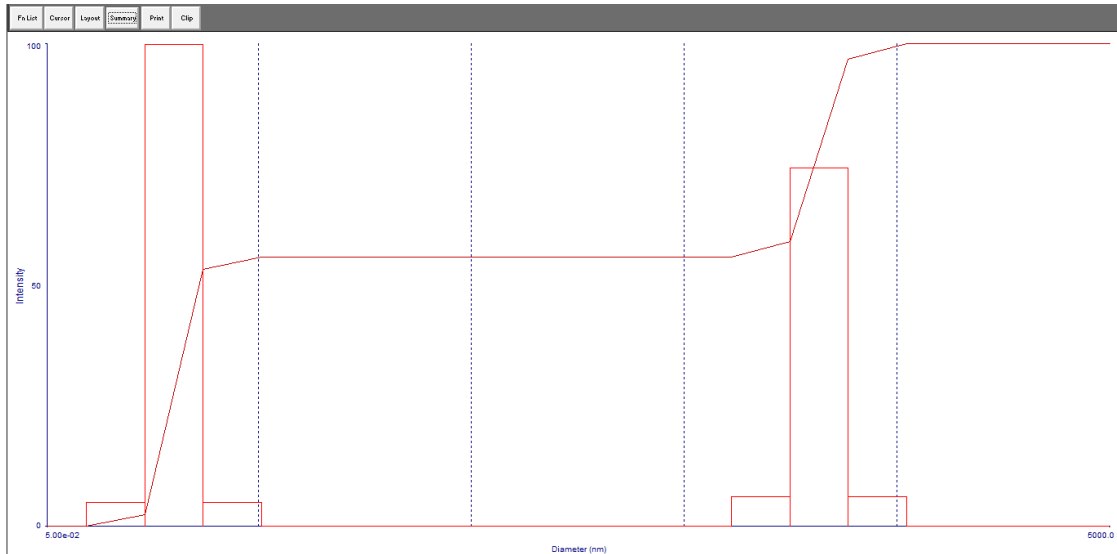


Figure 4.5: Bimodal particle size distribution example.

4.4 Kinetics of Humin Growth

The results of this section stem from several simplifying assumptions that are made during the analysis and interpretation. The first assumption made is that the growth kinetics follow a power law model. The second assumption is that any particles that form are perfect solid spheres, so that the volume can easily be calculated. A simple mass balance on the humins in the batch process is carried out below to exemplify the point.

$$\frac{dn}{dt} = M_h \frac{dm}{dt} = k_0 e^{-\frac{E_a}{RT}} \prod c_i^{a_i}$$

In the above equation, n is the number of moles of humins at any time t , M_h is the molecular weight of humins, k_0 is the kinetic pre-exponential factor, E_a is the

apparent activation energy, T is the temperature, c_i is the concentration of any reactant or product, and a_i is the order of reaction with respect to species i . The next equation introduces the particle diameter D that is being measured, and the particle density ρ .

$$\frac{dD}{dt} = \frac{k_0}{4\pi\rho M_h \left(\frac{D}{2}\right)^2} e^{-\frac{E_a}{RT}} \prod c_i^{a_i}$$

$$K = \frac{k_0}{4\pi\rho M_h \left(\frac{D}{2}\right)^2}$$

$$\ln\left(\frac{dD}{dt}\right) = \ln K - \frac{E_a}{RT} + \sum a_i \ln(c_i)$$

The final equation above shows a way to link the measurements obtained from the DLS with typical kinetic data that would be important to the catalysis community. The data obtained by utilizing this kinetic method are presented in Figure 4.6, Figure 4.7, and Figure 4.8. The linear fits were approximated for the first part of the data. In the figures below, it is clear that there is a time where the growth rate slows to a near stop. The error bars presented on the figures below correspond to standard deviations calculated from the population distribution obtained from the DLS software.

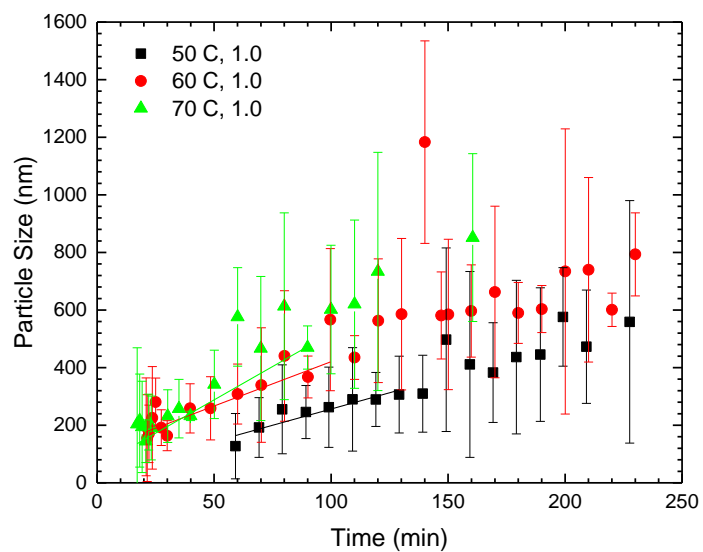


Figure 4.6: Dependence of humin growth rate on temperature at pH 1.0.

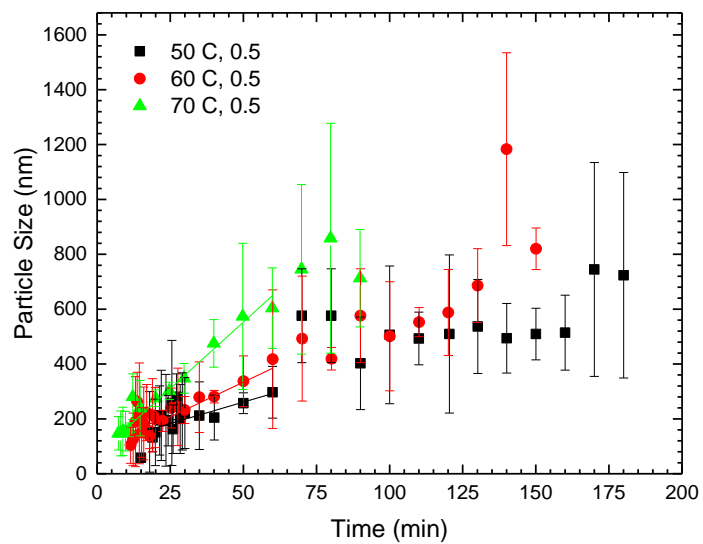


Figure 4.7: Dependence of humin growth rate on temperature at pH 0.5.

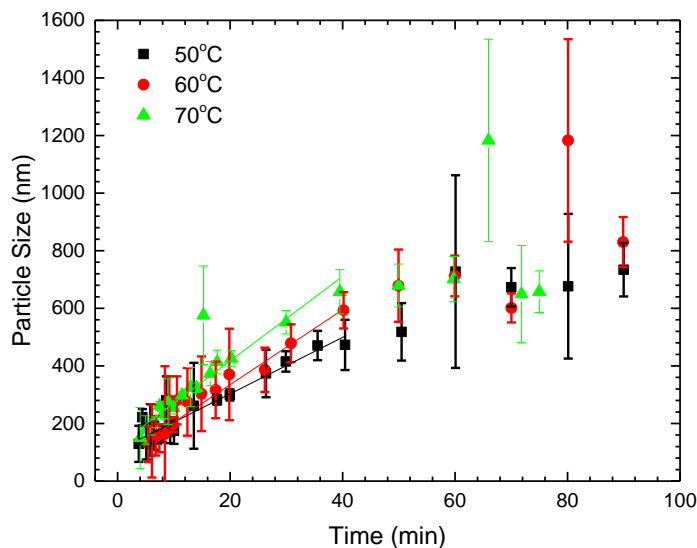


Figure 4.8: Dependence of humin growth rate on temperature at pH 0.0.

For each of these sets of data, the growth rate was approximated as a constant. The constant was obtained by fitting the diameter as a function of time to a straight line around the induction time. The slope for several sets varies slightly at the end, but this approximation will be enough for the analysis presented in this thesis. In the future, more complicated models will need to be built, reconciling molecular mechanisms with physical growth rates.

One piece of information that is critical to note in the DLS experimental data is the presence of growth only after particles of a critical “nucleus” has formed. The induction time, or time it takes to form the first critical particle, seems to correlate well with reaction conditions. For the purposes of this thesis, the induction time is defined as the time to form the first particle with a non-zero diameter. The correlation for induction times is shown in Figure 4.9.

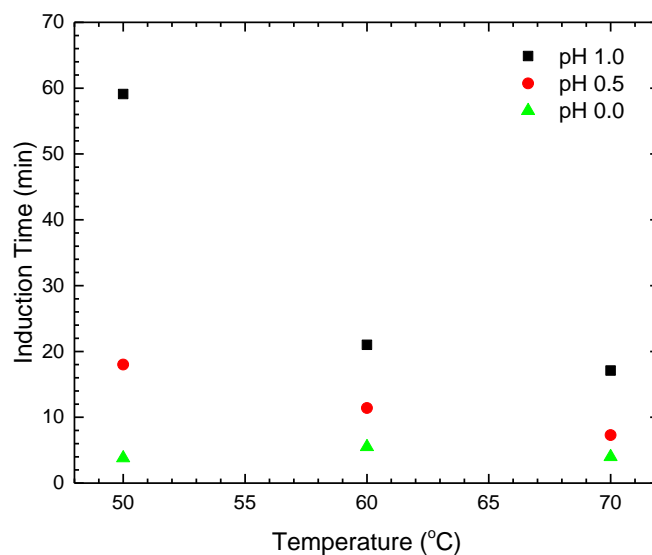


Figure 4.9: Correlation for humin induction time.

After the induction time had passed, the linear growth rate was measured, and the growth rate also correlates well with reaction conditions to match previous kinetic understanding and the induction time correlation. For example, we know that induction time is longest for high pH and low temperature, so we might expect those conditions to have slowest reaction, which they do. The reaction rates under differing reaction conditions are shown in Figure 4.10.

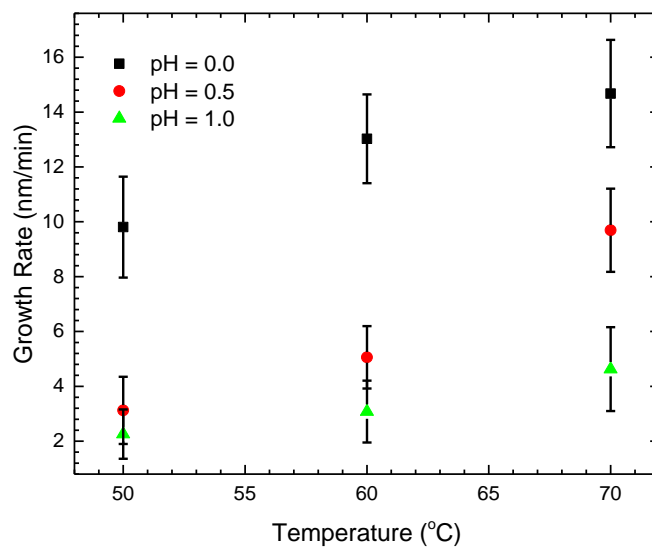


Figure 4.10: Humin linear growth rates correlated with reaction conditions. The error bars indicated here refer to 95% confidence interval in the slope of the fit.

Now that values for the linear growth rates have been obtained, the previously derived equations can be used to fit the data. When an Arrhenius plot, shown in Figure 4.11, is made with this data, the activation energy is found to be much lower than what has been observed previously.

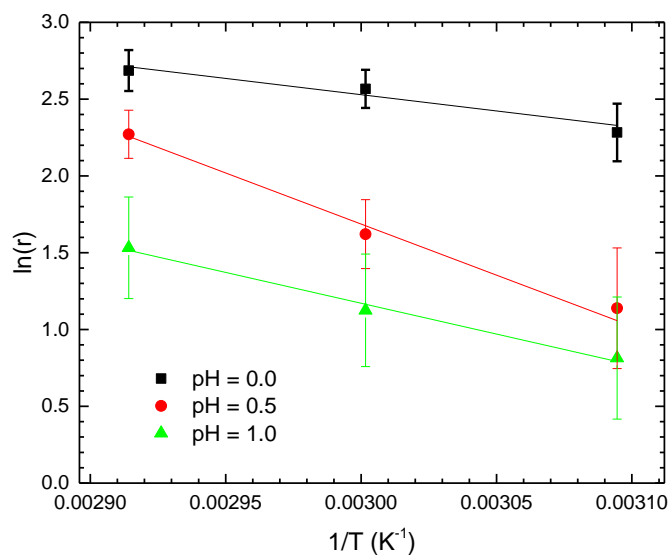


Figure 4.11: Arrhenius plot of DLS experiments

Table 4.6, below shows the values that were measured from the humin formation reactions using *in situ* DLS. Because of the small amount of data collected, these values have confidence intervals from the fits that are 100% or greater. For this reason, there needs to be a larger set of temperatures collected before trustworthy activation predictions can be made.

Table 4.6: Apparent activation energy measured from dynamic light scattering experiments.

pH	E_a^{app} (kJ/mol)
0.0	18.1
0.5	55.3
1.0	33.4

Previous literature has cited activation barriers on the order of 90 - 120 kJ/mol [19, 24, 25] while the activation energy we have directly measured is much smaller than that. Other sources have measured activation energies between 50 – 65 kJ/mol [26, 27], but our activation energies are still smaller by a factor of 1.5 to 2. This difference could be ascribed to the large errors present in our Arrhenius plot, because of the limited set of data that is used to build it. Another difference that could account for this discrepancy is the direct measurement of humin formation, instead of indirectly measuring the formation of other products and modelling the balance as humins. Depending on the mechanism of humin formation, the values could be significantly different when approximated by closing the mass balance or by direct measurement. However, the most likely source of error in measuring the activation energies is the presence of transport effects. During these experiments, it is not possible to mix the reactants, due to the disturbance that would be generated in the DLS measurement. This introduces significant transport effects, where the reactants need to diffuse to the location of a humin particle for the reaction to occur. If the diffusion time scale is compared to the reaction time scale, I would expect to find that the reaction times are much shorter. This would indicate the need to incorporate an effectiveness factor into the rate equation. This effectiveness factor is usually a function of the Thiele modulus, which compares the reaction time scale to diffusion time scale. If the Thiele modulus is large, the reaction is diffusion limited, and the measured activation energy will not be the actual activation energy for the reaction.

In order to validate these experiments, two sets of replicate data for one of the data points were measured. However, at this point, the replicate data do not agree with

each other. There is still explanation being sought as to why there is so much trouble to replicate the results. The replicate experiments are shown in Figure 4.12.

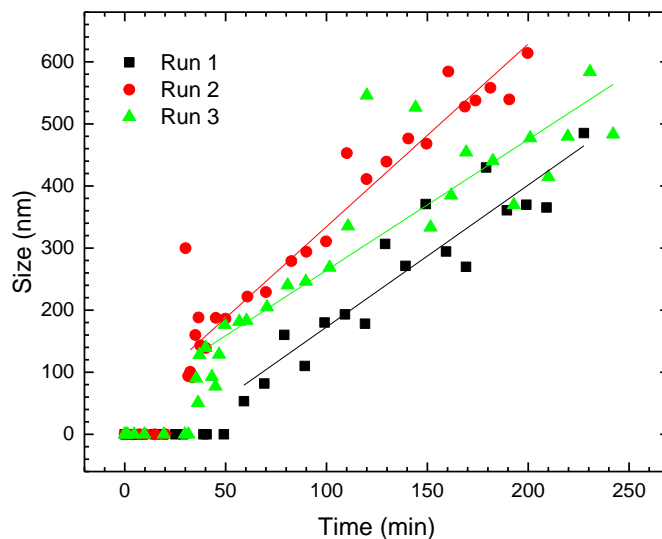


Figure 4.12: Replicate data for the DLS experiment at pH 1.0 and 50°C.

The slopes generated from the data fit are presented in Table 4.7. Although the expected value of the growth rate is different, the confidence intervals do overlap. This indicates that they are not statistically different measurements, even though they appear to be so different.

Table 4.7: Growth rate of humin particles as measured in replicate experiments. Error bars correspond to 95% confidence intervals.

Run #	Growth rate (nm/min)
1	2.2 ± 0.5
2	2.9 ± 0.3
3	2.1 ± 0.4

Chapter 5

FUTURE WORK AND CONCLUSIONS

This work has made some significant advances over the current literature in determining the molecular structure of the humins using IR spectroscopy. We have shown that the humin spectra depends heavily on how much the humins are washed, due to the adsorption of products on the humin particle. In addition, we have found that the humin structure depends on the starting material. We have found that there is a peak at 1650 cm^{-1} not explained in the literature that consistently appears in our humins formed from HMF, but not in the humins from fructose or glucose. This caused us to examine the humin structure as a function of conversion, and we found that this peak was consumed over the course of reaction. We compared the main structures found in literature to all of the data that was collected over the course of this thesis. This has led us to believe that the humin structure proposed by Weckhuysen and by Lund are the most likely candidates for the actual structure. Despite all of this, we are still uncertain what the true structure is, and more importantly what the formation mechanism is. To begin a study of the kinetics of this formation, we developed a novel technique using *in situ* DLS measurements for measuring growth rates and estimating activation energies. Our activation energies are much lower than other literature reported values. A complete reaction mechanism will be necessary to tie together the two pieces of this work, and is where the majority of questions still remain.

Although this project has made great headway in determining the most feasible structures of those proposed in the current literature, and in utilizing a novel technique for humin growth determination, the work is only just beginning. Perhaps fortunately, this thesis has raised more questions than it has answered. At this point, the studies will begin focusing on combining the information that our group and others have put together to work out detailed mechanistic models. The development of sophisticated models pairing the physical and chemical phenomena occurring in this problem will greatly aid in humin prevention. However, before those models can be developed, much more work needs to go into developing a mechanistic understanding of the humin formation. These could possibly take place as isotope labelling experiments, *in situ* IR experiments, and many others. These experiments can provide valuable insights into the formation mechanism of humins and possible ideas for humin reduction.

REFERENCES

1. Wang, T.; Nolte, M. W.; Shanks, B. H. Catalytic dehydration of C-6 carbohydrates for the production of hydroxymethylfurfural (HMF) as a versatile platform chemical. *Green Chem.* **2014**, *16*, 548-572.
2. van Putten, R.; van, d. W.; de Jong, E.; Rasrendra, C. B.; Heeres, H. J.; de Vries, J. G. Hydroxymethylfurfural, A Versatile Platform Chemical Made from Renewable Resources. *Chem. Rev.* **2013**, *113*, 1499-1597.
3. Vlachos, D. G.; Chen, J. G.; Gorte, R. J.; Huber, G. W.; Tsapatsis, M. Catalysis Center for Energy Innovation for Biomass Processing: Research Strategies and Goals. *Catal. Lett.* **2010**, *140*, 77-84.
4. Girisuta, B.; Janssen, L. P. B. M.; Heeres, H. J. Green Chemicals: A Kinetic Study on the Conversion of Glucose to Levulinic Acid. *Chem. Eng. Res. Design* **2006**, *84*, 339-349.
5. Leonard, R. H. Levulinic acid as a basic raw material. *Industrial and Engineering Chemistry* **1956**, *48*, 1331-1341.
6. Gallo, J. M. R.; Alonso, D. M.; Mellmer, M. A.; Dumesic, J. A. Production and upgrading of 5-hydroxymethylfurfural using heterogeneous catalysts and biomass-derived solvents. *Green Chem.* **2013**, *15*, 85-90.
7. Balakrishnan, M.; Sacia, E. R.; Bell, A. T. Etherification and reductive etherification of 5-(hydroxymethyl)furfural: 5-(alkoxymethyl)furfurals and 2,5-bis(alkoxymethyl)furans as potential bio-diesel candidates. *Green Chem.* **2012**, *14*, 1626-1634.
8. Nikbin, N.; Do, P. T.; Caratzoulas, S.; Lobo, R. F.; Dauenhauer, P. J.; Vlachos, D. G. A DFT study of the acid-catalyzed conversion of 2,5-dimethylfuran and ethylene to p-xylene. *Journal of Catalysis* **2013**, *297*, 35-43.
9. Williams, C. L.; Chang, C. -.; Do, P.; Nikbin, N.; Caratzoulas, S.; Vlachos, D. G.; Lobo, R. F.; Fan, W.; Dauenhauer, P. J. Cycloaddition of biomass-derived furans for catalytic production of renewable p-xylene. *ACS Catal.* **2012**, *2*, 935-939.

10. Do, P. T. M.; McAtee, J. R.; Watson, D. A.; Lobo, R. F. Elucidation of Diels-Alder Reaction Network of 2,5-Dimethylfuran and Ethylene on HY Zeolite Catalyst. *ACS Catal.* **2013**, *3*, 41-46.
11. Rosatella, A. A.; Simeonov, S. P.; Frade, R. F. M.; Afonso, C. A. M. 5-Hydroxymethylfurfural (HMF) as a building block platform: Biological properties, synthesis and synthetic applications. *Green Chem.* **2011**, *13*, 754-793.
12. Rinaldi, R.; Palkovits, R.; Schüth, F. Depolymerization of Cellulose Using Solid Catalysts in Ionic Liquids. *Angewandte Chemie International Edition* **2008**, *47*, 8047-8050.
13. Choudhary, V.; Mushrif, S. H.; Ho, C.; Anderko, A.; Nikolakis, V.; Marinkovic, N. S.; Frenkel, A. I.; Sandler, S. I.; Vlachos, D. G. Insights into the Interplay of Lewis and Bronsted Acid Catalysts in Glucose and Fructose Conversion to 5-(Hydroxymethyl)furfural and Levulinic Acid in Aqueous Media. *J. Am. Chem. Soc.* **2013**, *135*, 3997-4006.
14. Roman-Leshkov, Y.; Barrett, C. J.; Liu, Z. Y.; Dumesic, J. A. Production of dimethylfuran for liquid fuels from biomass-derived carbohydrates. *Nature* **2007**, *447*, 982-985.
15. Tsilomelekis, G.; Josephson, T. R.; Nikolakis, V.; Caratzoulas, S. Origin of 5-Hydroxymethylfurfural Stability in Water/Dimethyl Sulfoxide Mixtures. *ChemSusChem* **2014**, *7*, 117-126.
16. Lin, Z.; Ierapetritou, M.; Nikolakis, V. Aromatics from Lignocellulosic Biomass: Economic Analysis of the Production of p-Xylene from 5-Hydroxymethylfurfural. *AIChE J.* **2013**, *59*, 2079-2087.
17. Horvat, J.; Klaić, B.; Metelko, B.; Šunjić, V. Mechanism of levulinic acid formation. *Tetrahedron Lett.* **1985**, *26*, 2111-2114.
18. Van Zandvoort, I.; Wang, Y.; Rasrendra, C. B.; van'Eck, E. R. H.; Buijninx, P. C. A.; Heeres, H. J.; Weckhuysen, B. M. Formation, Molecular Structure, and Morphology of Humins in Biomass Conversion: Influence of Feedstock and Processing Conditions. *ChemSusChem* **2013**.
19. Patil, S. K. R.; Lund, C. R. F. Formation and Growth of Humins via Aldol Addition and Condensation during Acid-Catalyzed Conversion of 5-Hydroxymethylfurfural. *Energy Fuels* **2011**, *25*, 4745-4755.

20. Patil, S. K. R.; Heltzel, J.; Lund, C. R. F. Comparison of Structural Features of Humins Formed Catalytically from Glucose, Fructose, and 5-Hydroxymethylfurfuraldehyde. *Energy Fuels* **2012**, *26*, 5281-5293.
21. Sumerskii, I. V.; Krutov, S. M.; Zarubin, M. Y. Humin-like substances formed under the conditions of industrial hydrolysis of wood. *Russian Journal of Applied Chemistry* **2010**, *83*, 320-327.
22. Gunzler, H.; Gremlich, H. *IR Spectroscopy An Introduction*; Wiley - VCH: Weinheim, Germany, 2002; pp 361.
23. Nakanashi, K.; Solomon, P. H. *Infrared Absorbtion Spectroscopy*; Holden-Day: San Francisco, 1977; pp 287.
24. Swift, T. D.; Bagia, C.; Nikolakis, V.; Vlachos, D. G.; Peklaris, G.; Dornath, P.; Fan, W. Reactive adsorption for the selective dehydration of sugars to furans: Modeling and experiments. *AIChE J.* **2013**.
25. Girisuta, B.; Janssen, L. P. B. M.; Heeres, H. J. *Green Chem.* **2006**, *8*, 701.
26. Baugh, K. D.; McCarty, P. L. *Biotechnol. Bioeng.* **1988**, *31*, 50.
27. Swift, T. D.; Bagia, C.; Choudhary, V.; Peklaris, G.; Nikolakis, V.; Vlachos, D. G. Kinetics of Homogeneous Brønsted Acid Catalyzed Fructose Dehydration and 5-Hydroxymethyl Furfural Rehydration: A Combined Experimental and Computational Study. *ACS Catal.* **2014**, *4*, 259-267.
28. Robinson, R. A.; Stokes, R. H. *Electrolyte Solutions*; Butterworths: London, 1968.
29. Pecora, R., Ed.; In *Dynamic Light Scattering: Applications of Photon Correlation Spectroscopy*; Plenum Press: New York, 1985; pp 420.

Appendix A

BUFFER PREPARATION

Although a buffer prepared from HCl/KCl is not very common, the activity effects present in the ionic solution can be used to provide limited buffering ability. The recipe for these buffer solutions was found in the text by Robinson and Stokes [28]. The recipe was tested by measuring the pH of the resulting solution, and it was always found to be within 0.03 pH units of the nominal value. The recipe is presented in the table below as the amount of 0.2M HCl solution to be added to 50mL of 0.2M KCl solution to produce a total of 200mL of buffer.

Table A.1: Buffer recipe for HCl/KCl buffer used in FTIR experiments.

Desired pH	Volume of 0.2M HCl necessary (mL)
1.00	134
1.50	41.4
2.00	13.0

Appendix B

HPLC CALIBRATION CURVES

The curves presented in this appendix show the HPLC calibrations that were used for the analysis of liquid products during reaction. These calibrations were made after diluting a sample of known concentration. The fit on all of the curves was very good, with a coefficient of determination of 0.999 or greater.

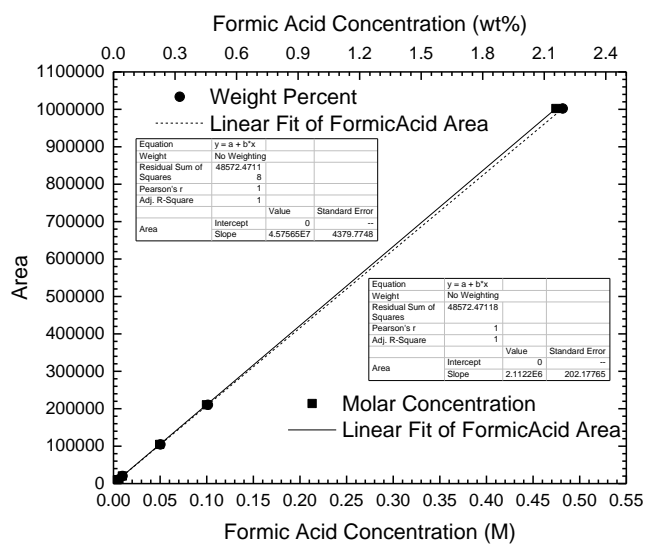


Figure B.1: HPLC calibration for formic acid.

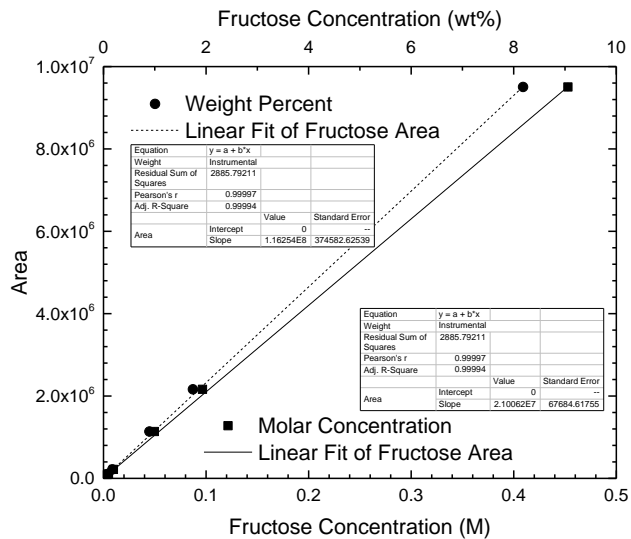


Figure B.2: HPLC calibration for fructose.

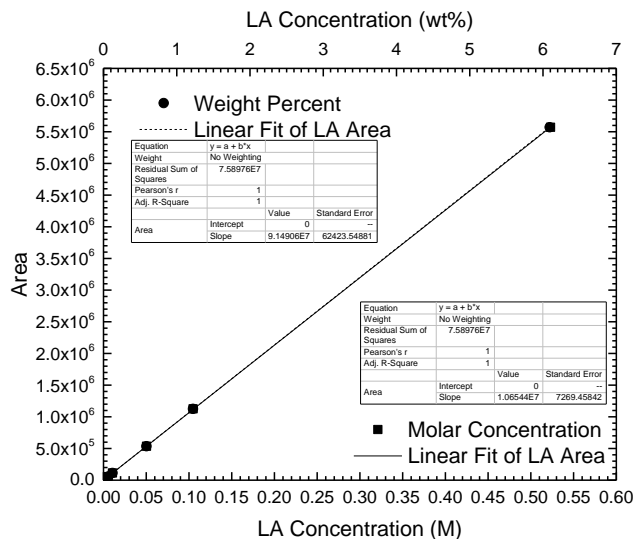


Figure B.3: HPLC calibration for levulinic acid.

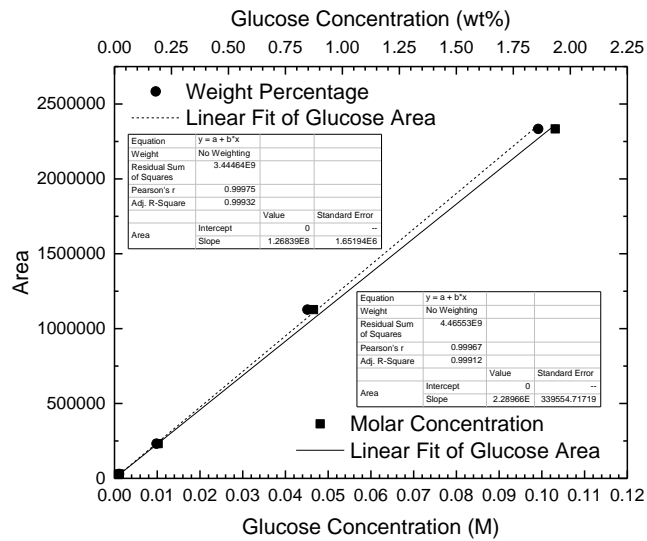


Figure B.4: HPLC calibration for glucose.

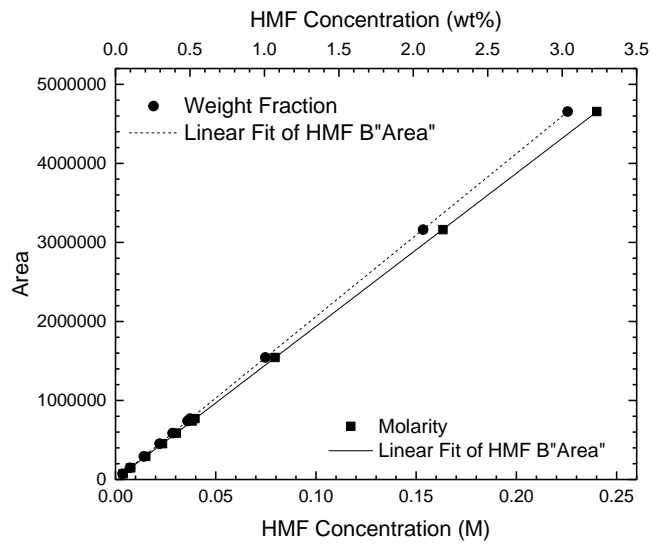


Figure B.5: HPLC calibration for HMF.

Appendix C

THEORY OF INFRARED SPECTROSCOPY

The theoretical basis for infrared spectroscopy has many foundations in the quantum mechanical description of molecules. Each particle in the molecule must satisfy the Schrödinger equation that balances the energy in the system. The most general form of the Schrödinger equation uses eigenvalue operators to describe the wave nature of particles at the quantum scale.

$$\hat{H}\psi = E\psi$$

The Hamiltonian operator, H , combines potential energy and kinetic energy to find the total energy that is being experienced by a particle in a system. For most applications of the Schrödinger equation, the potential field that can be solved analytically must be simplified greatly. This is also the case for IR systems. In this case, a molecule is approximated as a set of masses connected by springs. In this model, the potential field is well known from classical mechanics as being:

$$U(x) = \frac{1}{2}kx^2$$

where x is the distance from equilibrium. However, there is not a continuum of allowable energies that the molecule can have, so each vibration has a specific, quantized, amount of energy. As infrared light hits the molecule, it excites a motion with the precise amount of energy that is contained in the photon. The molecule then jumps from one energy level to the next, absorbing the incoming energy. This absorption of light is directly measured by the detector in the instrument.

With this harmonic oscillator approximation of atomic interactions, we can use classical mechanics to obtain the frequency of the induced vibration as

$$\nu = \frac{1}{2\pi} \sqrt{\frac{k}{\mu}}$$

where k is the force constant of the bond, and μ is the reduced mass of the two particles. As each bond in a molecule will have a unique force constant, the interaction of IR light with a given sample will give a unique description of the chemical composition. For this reason, IR spectroscopy is incredibly powerful as an analytical tool. There are many texts with more detailed description of the background of IR, but further analysis is beyond the scope of this text.

Appendix D

FTIR VIBRATIONAL TABLES

The tables presented in this section are a combination of the vibrational tables found in Nakanishi and Solomon's *Infrared Absorption Spectroscopy* and Günzler and Gremlich's *IR Spectroscopy: An Introduction*. These texts describe the methods used to qualitatively analyze any collected IR spectrum. This approach was what was followed throughout this work. The tables are presented as the possible groups that could occur that contain a common band seen in the IR spectrum. For this report, the bands that are included are the carbonyl band, the alkenyl band, the alcohol band, the ether band, and the acetal bands.

Table D.1: Carbonyl band vibrational frequencies.

Group	Frequency (cm ⁻¹)	Comments
-CH ₂ -C(=O)-CH ₂ -	1725 – 1700 [22, 23]	Strong intensity
-CH=CH-C(=O)-CH ₂ -	1695-1660 [22, 23]	Additional band of C=C shows 1650 – 1600' cm ⁻¹
Ar-C(=O)-CH ₂ -	1700-1680 [22, 23]	
-CH=CH-C(=O)-CH=CH-	1665 [23]	
-CH=CH-CH=CH-C(=O)-CH ₂ -		
Ar-C(=O)-Ar		
7-member C(=O)	1705 [23]	
6-member C(=O)	1715 [23]	
5-member C(=O)	1745 [23]	
4-member C(=O)	1780 [23]	
3-member C(=O)	1850 [23]	
-CH ₂ -C(=O)-H	1740 – 1720 [22, 23]	2850 – 2820, 2750 – 2720 band due to Fermi resonance of δC-H and

		ν C-H
-CH ₂ -C(=O)-OH	1760-1700 [22, 23]	Much stronger intensity than the ketone carbonyl

Table D.2: Alkane band vibrational frequencies.

Group	Frequency (cm ⁻¹)	Comments
-CH ₃	2960	Anti-symmetric stretching, strong peak
	2870	Symmetric stretching, medium absorbtivity
	1470	Anti-symmetric bending
	1380	Symmetric bending, doublet in geminal dimethyl groups
-CH ₂ -	2930-2925	Anti-symmetric stretching, strong
	2850	Symmetric stretching
	1470	Scissoring
	720	CH ₂ rocking

Table D.3: Alkyne band vibrational frequencies.

Group	Frequency (cm ⁻¹)	Comments
-C=C-	1650	Stretching, changes because of substitution
=CH ₂	3080	Symmetric stretching
	3010 – 2975	Anti-symmetric stretching
=CH-	3030 – 3020	C-H stretching
R/CH=CH ₂	1645	Alkene stretching
	1420 – 1415	C-H bending (in-plane)
	990, 910	C-H bending (out-of-plane)
R ₁ ,R ₂ C=CH ₂	1655	Alkene stretching
<i>cis</i> alkene	1660	Alkene stretching
<i>trans</i> alkene	1675	Alkene stretching

In the following table, the data presented refer to free OH and bonded OH. The free OH are those that are not taking place in any intermolecular hydrogen bonding. Because of this, the strength of the O-H bond is not changed that much. However, when hydrogen bonding is present in the compound, there will be a slight weakening of the O-H bond as electrons rearrange to minimize energetic interactions.

Table D.4: Alcohol band vibrational frequencies.

Group	Frequency (cm ⁻¹)	Comments
1° -OH	3640	OH stretch, free
	1075 – 1000	CO stretch
2° -OH	3630	OH stretch, free
	1120 – 1090	CO stretch
3° -OH	3620	OH stretch, free
	1210 – 1100	CO stretch
Ar-OH	3615 – 3590	OH stretch, free
	1260 – 1180	CO stretch
H-bonded	3400 – 3200	Strong absorption, broad peak

Table D.5: Ether/acetal band vibrational frequencies.

Group	Frequency (cm ⁻¹)	Comments
-C-O-C-	1150 – 1070	Anti-symmetric stretching
=C-O-C-	1275 – 1200	Anti-symmetric stretching
	1075 – 1020	Symmetric stretching
-C-O-C-O-C-	1200 – 1030	4 bands

Appendix E

THEORETICAL BACKGROUND OF DYNAMIC LIGHT SCATTERING

The background for this section is based on the work edited by Pecora [29]. Light scattering experiments can be used to measure many important parameters of colloidal suspensions. In dynamic light scattering, this is typically the diffusivity of particles in a solvent. The basis for these experiments is the random walk, or Brownian model of particle diffusion. In this model, a particle that is much larger than any of the solvent molecules surrounding it will have a probabilistic distribution of its position. When incident light interacts with these particles, the light will scatter at an angle off the particle. For very small particles, the scattering angle does not change the intensity of light scattered. However, for the particles that we are studying, scattering angle will make a significant impact.

In dynamic light scattering experiments, the fluctuations in the intensity of the scattered light is measured. These fluctuations can be used to calculate the particle diffusivity. The light source must be a highly focused, polarized source. When the intensity is measured, the autocorrelation function can be calculated as:

$$G_2(\tau) = \langle I(t)I(t + \tau) \rangle$$

Unfortunately, there isn't a direct relationship between the intensity of scattered light, and a particle diffusivity. To achieve this type of relationship, the scattered electric field autocorrelation needs to be incorporated.

$$G_1(\tau) = \langle E(t)E(t + \tau) \rangle$$

$$G_1(\tau) = Nb^2 e^{-Dq^2\tau}$$

This shows the dependence of the scattered electric field on the particle diffusivity, which can be related to the particle size using the Einstein-Stokes relationship:

$$D = \frac{k_B T}{6\pi\mu r}$$

By combining the autocorrelation for scattered light intensity, that is directly measured by the correlator, with the electric field autocorrelation results, we see that:

$$G_2(\tau) = G_1(0)^2 + G_1(\tau)^2$$
$$G_2(\tau) = B[1 + \beta e^{-2q^2 D \tau}]$$

This model suggests that there are three parameters that need to be fit from experimental data. In reality there are a wide distribution of particle sizes and therefore a wide range of diffusivities. Because of this, there are many more complicated theoretical models that are used for the fitting of experimental data. The ones that we focus on in the discussion are the cumulant, CONTIN, and NNLS fits.

Appendix F

AUTOCORRELATION FUNCTIONS

The autocorrelation functions presented in this section are those obtained during reaction, but none prior to the formation of humin particles. This eliminates any of the autocorrelation functions that show no autocorrelation between the velocity. As the reaction time increases, the decay time also increases, indicating the presence of larger particles. This analysis assumes a constant viscosity throughout the course of the reaction.

F.1 T = 70°C

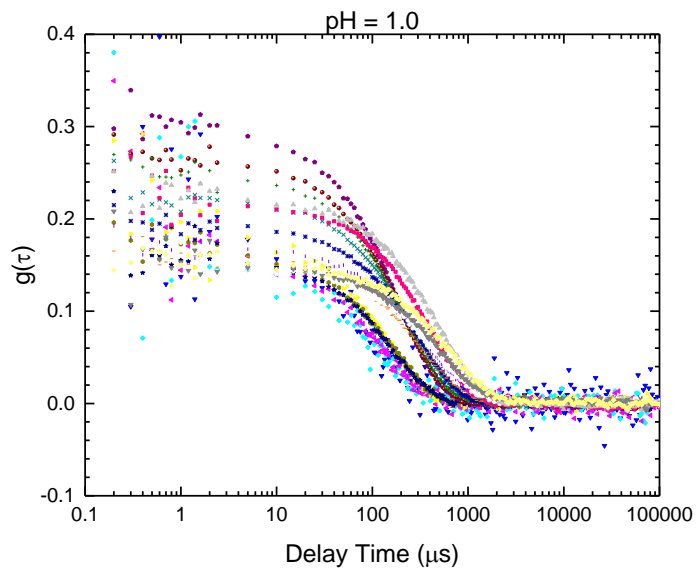


Figure F.1: Autocorrelation function of humins produced at 70°C and pH 1.0.

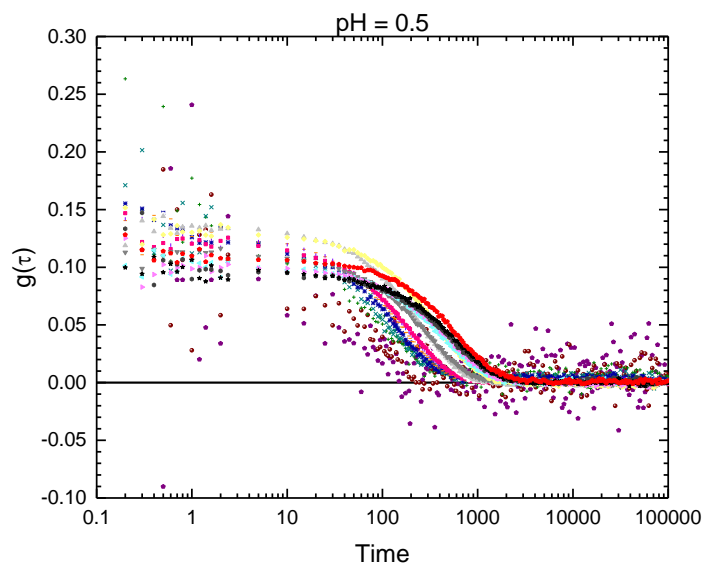


Figure F.2: Autocorrelation function of humins produced at 70°C and $\text{pH } 0.5$.

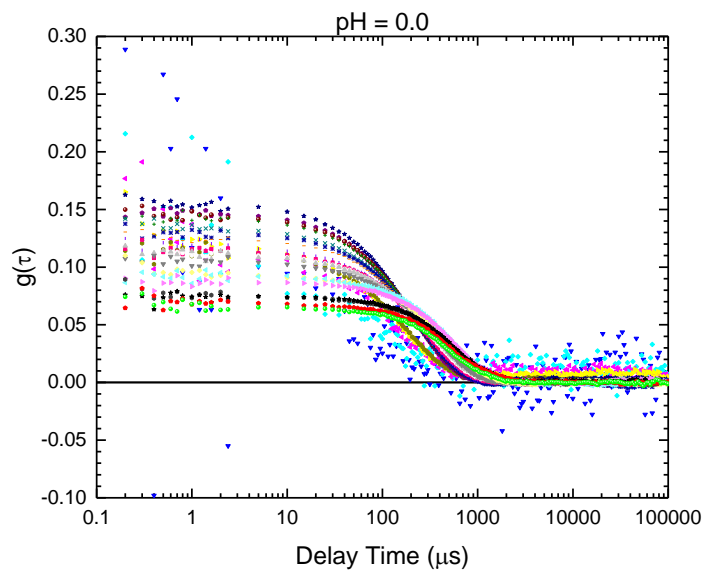


Figure F.3: Autocorrelation function of humins produced at 70°C and $\text{pH } 0.0$.

F.2 T = 60°C

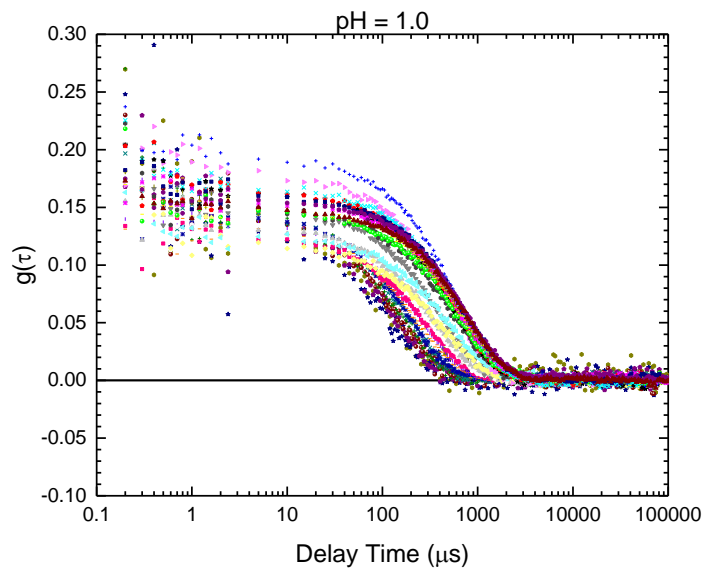


Figure F.4: Autocorrelation function of humins produced at 60°C and pH 1.0.

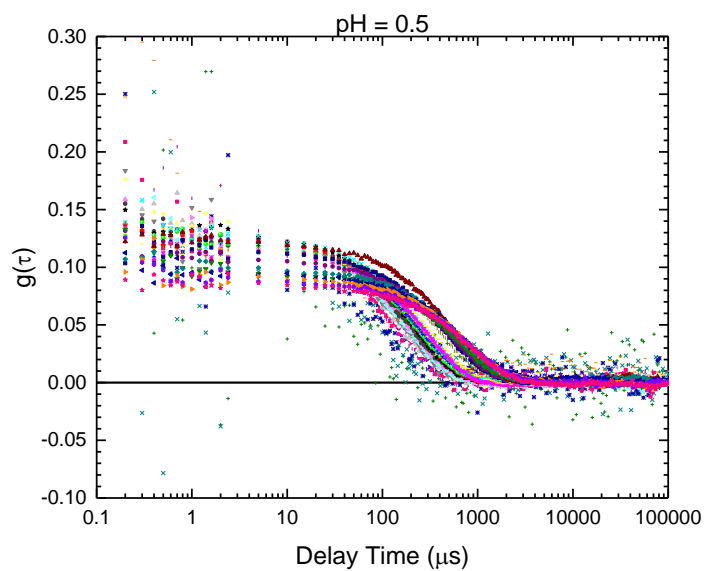


Figure F.5: Autocorrelation function of humins produced at 60°C and $\text{pH } 0.5$.

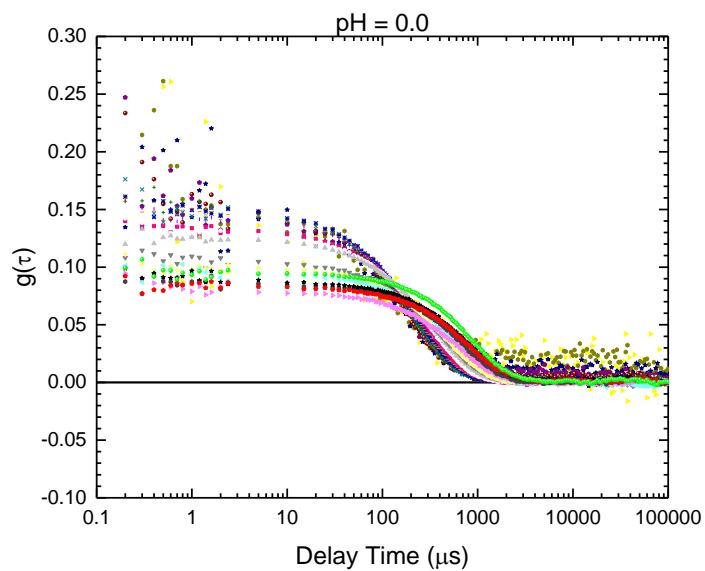


Figure F.6: Autocorrelation function of humins produced at 60°C and $\text{pH } 0.0$.

F.3 T = 50°C

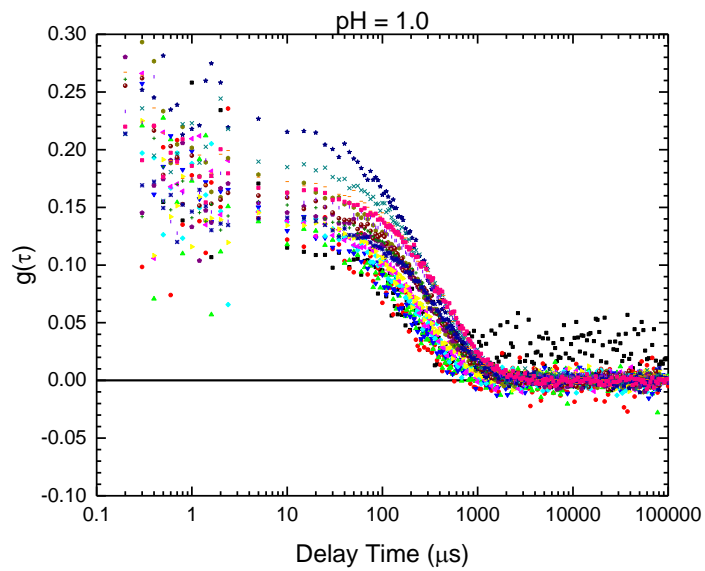


Figure F.7: Autocorrelation function of humins produced at 50°C and pH 1.0.

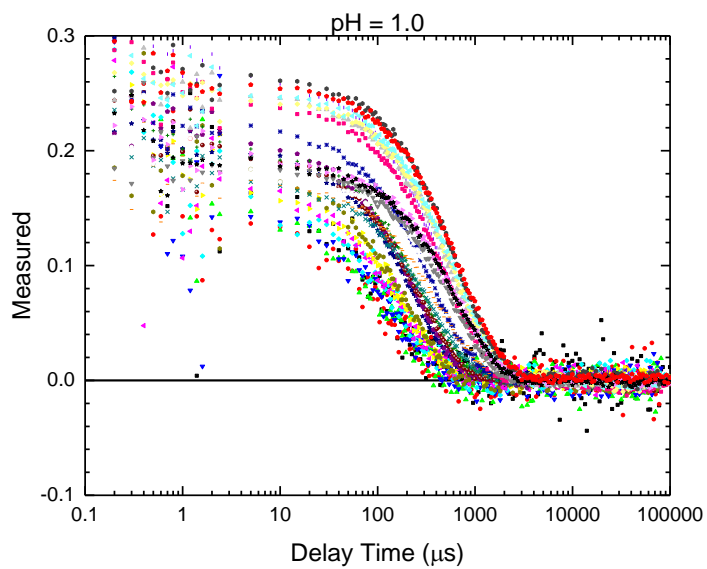


Figure F.8: Autocorrelation function of humins produced at 50°C and pH 1.0.

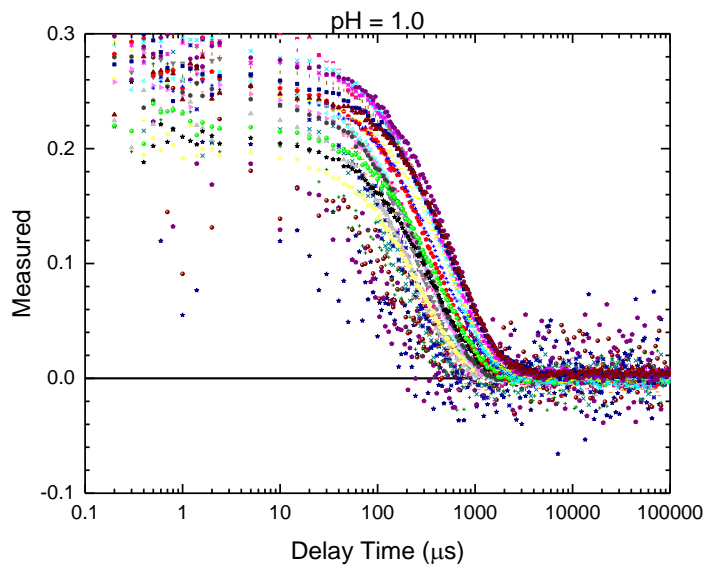


Figure F.9: Autocorrelation function of humins produced at 50°C and pH 1.0.

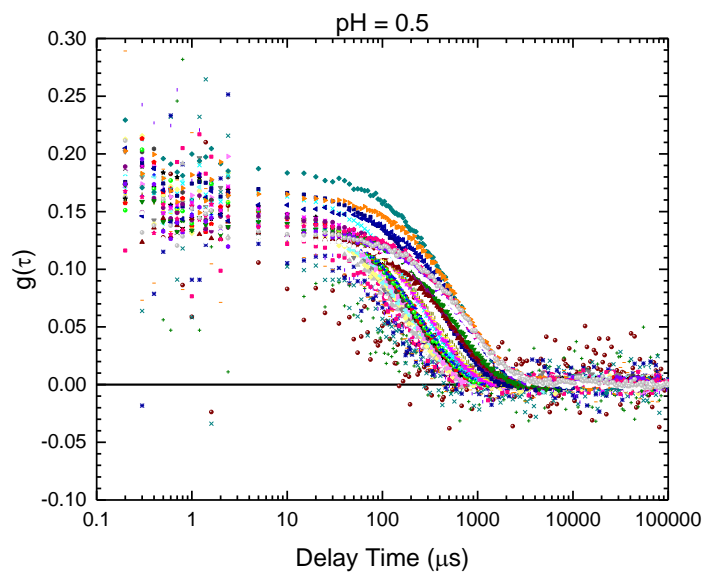


Figure F.10: Autocorrelation function of humins produced at 50°C and $\text{pH } 0.5$.

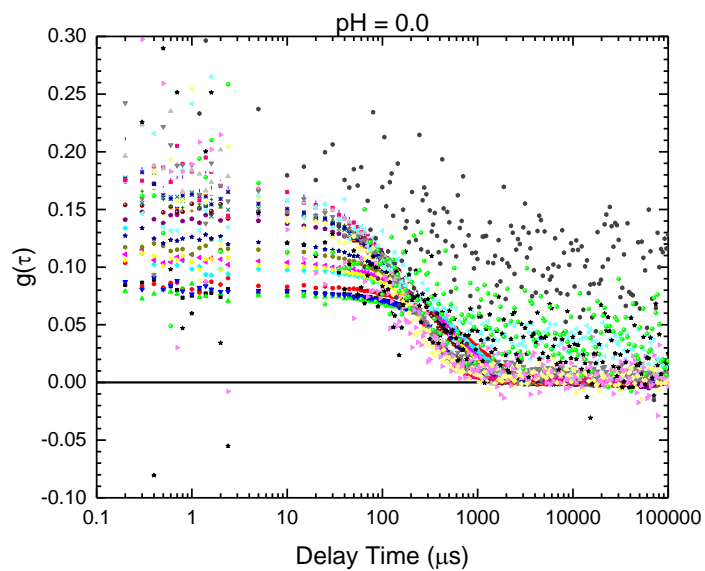


Figure F.11: Autocorrelation function of humins produced at 50°C and $\text{pH } 0.0$.